This Book of Proceedings contains the extended abstracts of the contributions presented at the DIPSI Workshop 2024 on Droplet Impact Phenomena and Spray Investigation, organized by the University of Bergamo on Friday 17th June 2024 in Bergamo, Italy.

This workshop, which is now at its sixteenth edition, represents an important opportunity to share the recent knowledge on droplets and sprays in a variety of research fields and industrial applications.

The event is supported by the Department of Engineering and Applied Sciences of the University of Bergamo and the Research Training Group 2160/2 DROPIT in collaboration with the University of Stuttgart.

GIANPIETRO ELVIO COSSALI **is full professor of Thermal Physics at the Department of Engineering and Applied Sciences of the University of Bergamo. His research activity is carried out in the field of thermo-fluid dynamics of multiphase systems, with particular reference to the characterization of sprays, to the dynamics of the interaction between droplets and solid and liquid surfaces and to the analytical modelling of heat and mass exchange in dispersed flows. He teaches the course of Thermal Physics, Thermo-fluid-dynamics and Heat transfer at the University of Bergamo.**

SIMONA TONINI **is is Associate Professor of Thermal Physics at the Department of Engineering and Applied Sciences of the University of Bergamo. His research is carried out in the field of theoretical and numerical modeling of transport phenomena in multiphase flows. She teaches the course of Thermal Physics and HVAC Systems and the course of Thermal Physics for Advanced Technology for the Engineering degrees at the University of Bergamo.**

ISBN: 978-88-97253-12-9
DOI: 10.13122/DIPSI2024

PROCEEDINGS OF THE DIPSI WORKSHOP 2024

PROCEEDINGS OF THE DIPSI WORKSHOP 2024

Droplet Impact Phenomena & Spray Investigations

BERGAMO, ITALY, 17th JUNE 2024

Edited by Gianpietro Elvio Cossali, Simona Tonini

UNIVERSITÀ DEGLI STUDI DI BERGAMO

2024

PROCEEDINGS
OF THE
DIPSI WORKSHOP 2024

Droplet Impact Phenomena
& Spray Investigations

BERGAMO, ITALY, 17th JUNE 2024

Edited by Gianpietro Elvio Cossali

Università degli Studi di Bergamo
2024

PROCEEDINGS OF THE DIPSI WORKSHOP 2024: Droplet Impact Phenomena & Spray investigations, Bergamo, Italy, 17th June 2024 / edited by Gianpietro Elvio Cossali – Bergamo: Università degli Studi di Bergamo, 2024.
ISBN: **978-88-97253-12-9**
DOI: **10.13122/DIPSI2024**

Progetto grafico:
Servizi Editoriali – Università degli Studi di Bergamo
Università degli Studi di Bergamo
via Salvecchio, 19
24129 Bergamo
Cod. Fiscale 80004350163
P. IVA 01612800167

https://aisberg.unibg.it/handle/10446/297385

Workshop agenda, Monday 17th June 2024

08:45 Registration

09:00 Welcome speech

09:15 S1 Numerical methods

9:15 M. Ibach, N. Roth, S. Tonini, G.E. Cossali, B. Weigand, *Numerical and Analytical Study of Large Amplitude Shape Oscillations of Viscous Droplets*

9:40 R. Tietz, S. Fasoulas, and M. Pfeiffer, *Enskog-Vlasov Simulations in High Pressure Environments*

10:05 Coffee break

10:50 S2 Drop/wall interaction

10:50 R. Akbari, P. Sartipizadeh, M. Reza Mohammadizadeh, C. Antonini, *Increasing fog harvesting efficiency through hydrophobizing steel meshes*

11:15 A. Sinhaa, A. Georgoulas, M. Santin, *Which wound dressing is better for rapid absorption of wound exudate?*

11:40 A. Amoresano, S. Roscioli, M. Dedes, *Characterisation of non-toxic hull paints by static and dynamic droplet impact investigation*

12:05 Lunch break

13:30 Poster session

J. Wurst, K. Schulte, *Simulation framework for drop impacts on structured surfaces using PLIC-based contact line modeling*

R. Saha, B. Weigand, DNS of droplet impact onto heated surfaces

A. K. Geppert, D. B. Brajer, M. Marengo, *Mechanism behind the Generation of a Rectangular Liquid Umbrella after Droplet Impact onto a Small Square Surface*

S.S. Sazhin, D.V. Antonov, E.M. Starinskaya, V. Terekhov, S.V. Starinskiy, *Heating and evaporation of sessile droplets: new models of the processes*

D. Klötzl, D. Weiskopf, *NMF-Based Analysis of Droplet Wall-Film Interactions*

R. Dhar, K. Schulte, *Investigation of droplet-pool phenomena and droplet-film interaction for immiscible fluids*

14:00 S3 Phase change

14:00 S.S. Sazhin, S. Tonini, G.E. Cossali, D.V. Antonov, P.A. Strizhak, *New approaches to modelling heat/mass transfer processes in spherical and non-spherical mono-component droplets*

14:25 V.Kunberger, B. Weigand, *The influence of heat transfer on the outcome of droplet collisions of supercooled water droplets*

14:50 S4 Drop Impact

14:50 P. Palmetshofer, B. Weigand, *Splashing modes in droplet impacts onto sub-millimeter microstructures*

15:15 J.L. Stober, K. Schulte, *Investigation of the Flow Field at the Wall during an Oblique Droplet Impact onto a Thin Wall Film*

16:15 Coffee break

16:30 Workshop closure

Bergamo, 17th June 2024

Contents

Numerical and Analytical Study of Large Amplitude Shape Oscillations of Viscous Droplets

M. Ibach*[1], N. Roth, S. Tonini[2], G.E. Cossali[2], B. Weigand[1]

[1]Institute of Aerospace Thermodynamics (ITLR), University of Stuttgart, Stuttgart, Germany
[2]Department of Engineering and Applied Sciences, Università degli Studi di Bergamo, Dalmine (BG), Italy
*Corresponding author: matthias.ibach@itlr.uni-stuttgart.de

Introduction

Droplet oscillations, despite being seemingly simple and inconspicuous, play a crucial role and significantly contribute to various natural and industrial processes. The mathematical foundation for understanding these oscillations was first theorized over 140 years ago by Lord Rayleigh [4] and has since become central to fluid dynamics research. Understanding droplet dynamics is crucial for optimizing many modern technical processes. Various theoretical models and experimental studies have investigated droplet oscillations across a range of conditions, from small deviations from the initial spherical shape with inviscid droplets to those with large amplitudes, high viscosity and nonlinear oscillation behavior [1, 3, 7, 9].
This study extends these seminal works by examining in detail the impact of the following three specific factors on droplet oscillations. First, large initial aspect ratios and amplitudes, denoted as $\varepsilon = R_{ax}/R_{rad}$. Second, it explores varying material properties, with particular focus on liquid viscosity characterized by the Ohnesorge number $Oh = \mu_l/\sqrt{\rho_l \sigma D_0}$. Finally, it investigates different initial droplet shapes, comparing ellipsoidal forms to spherical harmonics of order 2. The effects of these factors are analyzed in terms of oscillation frequency f, the time spent in prolate and oblate shapes t_p, t_o, and the total energy budget E_{tot} contained in these shapes. The primary goal is to present a novel methodology for analyzing data obtained from highly resolved direct numerical simulations (DNS) conducted with ITLR's Free Surface 3D (FS3D) multiphase flow solver, thereby facilitating the comparison and extension of existing analytical models and approaches.

Fundamentals and Computational Setup

This study utilizes the ITLR in-house multiphase code FS3D, which solves the incompressible Navier-Stokes equations via direct numerical simulations. The code employs a finite volume approach on a staggered Cartesian grid to conserve mass and momentum. The classical Volume-of-Fluid (VOF) method is used by introducing an additional scalar field denoting the volume fraction of the fluid in each computational cell to distinguish between the liquid (subscript l) and gaseous (subscript g) phases. An additional transport equation tracks the advection of the liquid phase. The Piecewise Linear Interface Calculation (PLIC) algorithm is applied to accurately capture the interface and minimize numerical diffusion. Complete volume conservation during advection is ensured by treating the dilatation term, which occurs due to the directional splitting of the transport equation, as proposed by Weymouth and Yu [8]. Both phases are treated as a single fluid in a one-field formulation, with physical properties calculated locally based on the local VOF-value of the scalar field. FS3D is fully parallelized with MPI and OpenMP, optimized to run efficiently on the HPE Apollo supercomputer *Hawk* at the High Performance Computing Center Stuttgart (HLRS), where all simulations for this study were performed. For additional details on the numerical methods and capabilities, see Eisenschmidt et al. [2].

For the numerical study of droplet oscillations in a gaseous surrounding environment, a three-dimensional cuboidal Cartesian grid is used. A single liquid droplet is centered in the domain, with boundary conditions set far from the droplet to avoid boundary effects. The droplet is resolved with 85 grid cells per diameter, as verified in Reutzsch et al. [5]. The boundary conditions are zero gradient, gravity is neglected and the balanced CSF (bCSF) surface tension model is employed. To induce oscillations, the droplet is initialized with shapes deviating from the spherical form, such as ellipsoids with aspect ratios $\varepsilon = R_{ax}/R_{rad}$ (where R_{ax} and R_{rad} are

the axial and radial radii, respectively) or higher-order Legendre polynomials. Material properties and parameter ranges for ε and Oh for the present study are given in Tab. 1.

The droplet shape oscillation data is analyzed by extracting the time spent in prolate (t_p, $\varepsilon > 1$) and oblate (t_o, $\varepsilon < 1$) shapes, as well as the oscillation frequency $f = 1/(t_o + t_p)$. Additionally, the energy budget, encompassing surface energy E_σ and kinetic energy E_{kin}, with total energy defined as $E_{tot} = E_\sigma + E_{kin}$, is tracked. Non-dimensional parameters are used for evaluation and plotting the results. These are for the time $\hat{t} = t/\tilde{t}$, for the frequency $\hat{f} = f/\tilde{f}$ and for the energy $\hat{E} = E/\tilde{E}$, using the following parameters for non-dimensionalization $\tilde{t} = \sqrt{\sigma/(\rho_l R_0^3)}$, $\tilde{f} = \sqrt{8\sigma/(\rho_l R_0^3)}/(2\pi)$ and $\tilde{E} = R_0^2\sigma$.

Results and Discussion

The left graphs of Fig. 1-3 quantify the investigated effects on the evolution of the nondimensional oscillation frequency $\hat{f}$ as a function of the droplet's instantaneous aspect ratio $\varepsilon > 1$. The top row illustrates the impact of increasing elongation/amplitude ε, the second row shows the influence of viscosity through the Ohnesorge number Oh and the third row compares the initial shapes of an ellipsoid with those of a spherical harmonic of order 2.

As ε decreases over time due to viscous damping, the oscillation period shortens, leading to an increase in frequency. Consequently, $\hat{f}$ increases and eventually converges non-monotonically towards $\hat{f} = 1$, aligning with predictions by [3, 9]. While this method of analyzing and plotting $\hat{f}$ over ε is well-established in literature, novel observations emerge in cases of large amplitudes, high viscosities and varying shapes. Specifically, for large amplitudes $\varepsilon > 1.5$, an spreading of curves and increase in frequency is observed, which deviates from predictions by linear theory or conventional models. Additionally, increasing Oh, which corresponds to higher liquid viscosity, results in a decreased oscillation frequency, particularly in the later stages of oscillation for $\varepsilon < 1.3$. When comparing a regular ellipsoid with a droplet initialized as a second harmonic, differences arise, with the second-order harmonics case displaying higher frequencies for the same initial elongation, particularly for $\varepsilon > 1.3$. This may be explained by nonlinearities and mode coupling between higher and lower oscillation modes.

Given that droplet oscillation dynamics are governed by the interplay of kinetic energy, surface tension and viscosity, which together dictate the droplet's shape and stability, analyzing this interaction by plotting the energy at specific phases (e.g., oblate or prolate) is insightful. This is illustrated in the right plots of Fig. 1-3, where the total nondimensional energy $\hat{E}_{tot}$ is plotted against $\hat{t}_o$ and $\hat{t}_p$. Remarkably, all cases (varying ε, Oh and initializations) consistently collapse onto a single curve. During the prolate phase ($\hat{t} > 1.12$), the time spent in this shape increases linearly with total energy $\hat{E}_{tot}$, correlating with an increase in droplet elongation ε. Conversely, in the oblate shape, $\hat{t}_o$ asymptotically approaches ≈ 0.98 as $\hat{E}_{tot}$ increases. Notably, for higher viscosities ($Oh \gtrsim 0.006$) and larger elongations for different initial shapes, deviations from this curve occur, which are not predicted by analytical models.

The right plot of Fig. 1 additionally shows results from an analytical model recently proposed in [6] that predicts the dynamics of an oscillating droplet in an immiscible fluid, by solving the mechanical energy balance over the droplet using a generalized curvilinear coordinate system. The model assumes irrotational potential flow in both the inner and outer fields, accounting

Table 1. Material properties of the liquid and the gaseous phase with the investigated ranges from the conducted simulations.

Liquid Properties				Gaseous Properties		Investigated Range	
ρ_l	μ_l	σ	D_0	ρ_g	μ_g	ε	Oh
$\mathrm{kg\,m^{-3}}$	$\mathrm{mPa\,s}$	$\mathrm{mN\,m^{-1}}$	mm	$\mathrm{kg\,m^{-3}}$	$\mathrm{mPa\,s}$	$-$	$-$
998.2	1.00153	72.75	1.000	1.204	0.01821	$1.05 - 2.5$	$5.9 \cdot 10^{-4} - 5.9 \cdot 10^{-2}$

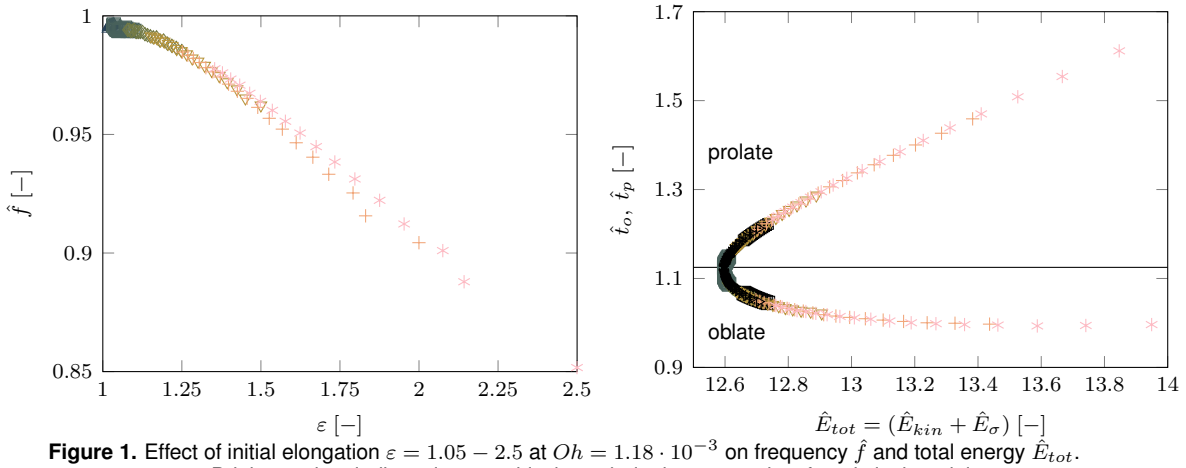

Figure 1. Effect of initial elongation $\varepsilon = 1.05 - 2.5$ at $Oh = 1.18 \cdot 10^{-3}$ on frequency $\hat{f}$ and total energy $\hat{E}_{tot}$. Brighter colors indicate larger ε, black symbols denote results of analytical model.

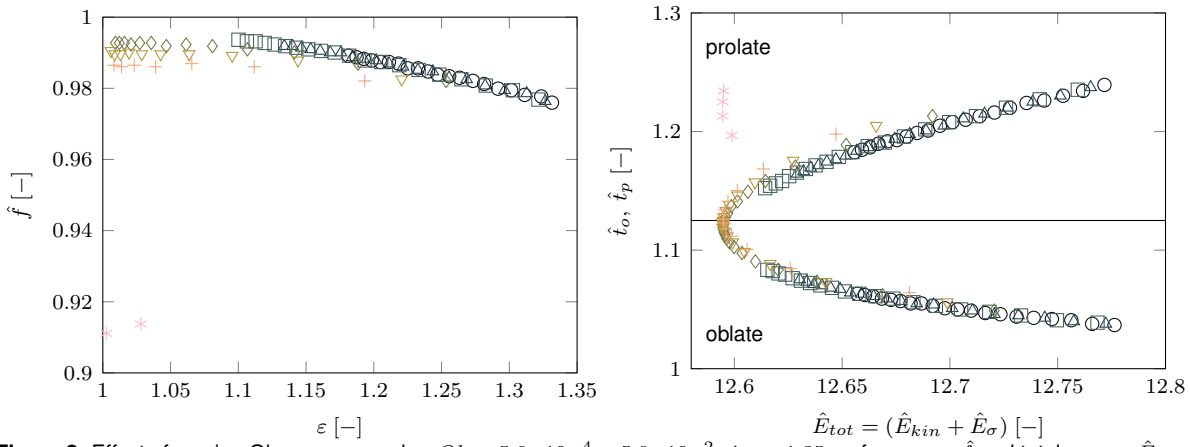

Figure 2. Effect of varying Ohnesorge number $Oh = 5.9 \cdot 10^{-4} - 5.9 \cdot 10^{-2}$ at $\varepsilon = 1.35$ on frequency $\hat{f}$ and total energy $\hat{E}_{tot}$. Brighter colors indicate larger Oh.

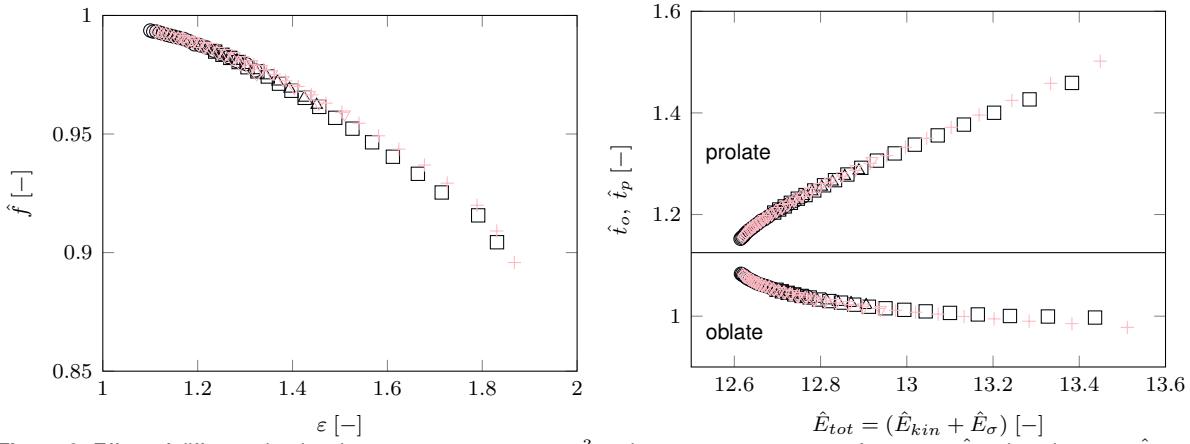

Figure 3. Effect of different droplet shapes at $Oh = 1.18 \cdot 10^{-3}$ and $\varepsilon = 1.35, 1.50, 2.00$ on frequency $\hat{f}$ and total energy $\hat{E}_{tot}$. The dark color indicates the initial ellipsoidal form, the bright color indicates the initial spherical harmonic of order 2.

for viscous dissipation. For small ε and Oh, the model agrees well with the results. However, deviations at larger amplitudes and viscosities may arise from mode coupling, where energy is transferred from higher modes to lower ones rather than being damped, leading to different energy distributions and, consequently, different prolate and oblate oscillation times.

Conclusion and Outlook

Analytical modeling often falls short in accurately predicting non-linear behavior or only capturing weakly non-linear phenomena. This study demonstrates that highly resolved numerical simulations, combined with appropriate data analysis, can effectively address these limitations, offering significant enhancements and extensions to available models methods. This study

introduced a novel approach for the detailed investigation of oscillating droplets, specifically focusing on cases with large amplitudes, highly viscous liquids and varying initial droplet shapes. The analysis revealed that by appropriately nondimensionalizing the data, a consistent collapse of data points is achieved when plotting the time droplets spend in prolate and oblate shapes against their total energy, encompassing both kinetic and surface energy. This collapse was observed across both numerical and analytical results within a specific range of conditions.

Nevertheless, several open questions remain that warrant further study, including a deeper investigation into the effects and discrepancies of varying initial droplet shapes (such as ellipsoids versus higher harmonics) on frequency variation and total energy, as well as a thorough exploration of the observed oblate/prolate asymmetry. Another important area for investigation is to uncover the underlying physical mechanisms that explain the observed patterns and the consistent collapse of data points in the plots of oscillation times versus total energy across different conditions. Additionally, it is crucial to reassess the assumption of potential flow within droplets in the analytical model, by using highly resolved DNS for comparison and flow visualization, as this can provide a more accurate depiction of the flow dynamics.

Nomenclature

D_0	droplet equivalent diameter [m]	ε	initial aspect ratio [$-$]
E	energy [(kg m^2)/s^2]	μ	dynamic viscosity [mPa s]
f	frequency [1/s]	ρ	density [kg/m^3]
Oh	Ohnesorge number [$-$]	σ	surface tension [N/m]
R_{ax}, R_{rad}	droplet (axial, radial) radius [m]	$\tilde{}$	non-dimensionalization factor
t_o, t_p	oblate, prolate time [s]	$\hat{}$	non-dimensional parameter

Acknowledgments

This work was funded by the Deutsche Forschungsgemeinschaft (DFG, German Research Foundation) in the scope of the International Research Training Group "Droplet Interaction Technologies" (GRK 2160/2: DROPIT) and under Germany's Excellence Strategy - EXC 2075 – 390740016. We also acknowledge the support by the Stuttgart Center for Simulation Science (SimTech) and the High Performance Computing Center Stuttgart (HLRS) for the support and the supply of computational resources on the HPE Apollo (Hawk) platform (FS3D/11142).

References

[1] E. Becker, W. J. Hiller, and T. A. Kowalewski. Experimental and theoretical investigation of large-amplitude oscillations of liquid droplets. *J Fluid Mech*, 231:189–210, 1991.

[2] K. Eisenschmidt, M. Ertl, H. Gomaa, C. Kieffer-Roth, C. Meister, P. Rauschenberger, M. Reitzle, K. Schlottke, and B. Weigand. Direct numerical simulations for multiphase flows: An overview of the multiphase code FS3D. *Appl Math Comput*, 272:508–517, 2016.

[3] A. Prosperetti. Free oscillations of drops and bubbles: the initial-value problem. *J Fluid Mech*, 100(2):333–347, 1980.

[4] J. W. S. Rayleigh. On the capillary phenomena of jets. *Proceedings of the Royal Society of London*, 29(196-199):71–97, 1879.

[5] J. Reutzsch, G. V. R. Kochanattu, M. Ibach, C. Kieffer-Roth, S. Tonini, G. E. Cossali, and B. Weigand. Direct Numerical Simulations of Oscillating Liquid Droplets: a Method to Extract Shape Characteristics. In: ILASS-Europe 2019.

[6] S. Tonini and G. E. Cossali. Analytical model of small- and large-amplitude drop oscillation dynamics. Submitted to Physics of Fluids, August, 2024.

[7] J. A. Tsamopoulos and R. A. Brown. Nonlinear oscillations of inviscid drops and bubbles. *J Fluid Mech*, 127:519–537, 1983.

[8] G. Weymouth and D. K.-P. Yue. Conservative Volume-of-Fluid method for free-surface simulations on Cartesian-grids. *Journal of Computational Physics*, 229(8):2853–2865, 2010.

[9] D. Zrnić, P. Berglez, and G. Brenn. Weakly nonlinear shape oscillations of a Newtonian drop. *Physics of Fluids*, 34(4):043103, 04 2022.

Enskog-Vlasov Simulations in High Pressure Environments

R. Tietz*[1], R. Stierle[2], F. Fasoulas[1], M. Pfeiffer[1]
[1]Institute of Space Systems, University of Stuttgart, Germany
[2]Institute of Thermodynamics and Thermal Process Engineering, University of Stuttgart, Germany
*Corresponding author: rtietz@irs.uni-stuttgart.de

Introduction

The climate crisis is one of the most challenging issues facing our society. Global carbon dioxide emissions must therefore be significantly reduced. One of the sectors with the least savings is transportation. Therefore, internal combustion engines must be replaced by electric alternatives, but where this is not possible, combustion must be made more efficient. This would reduce emissions (including soot) and conserve valuable fuels.
One idea by Lamanna et al. [8] is to improve the mixing of fuel with air. At present, small droplets of fuel are dispersed in the air during combustion, creating oxygen and fuel rich areas in the combustion chamber, which reduces efficiency. If the fuel is heated above its critical temperature, the liquid fuel droplets become supercritical and the mixing problem would become much simpler and more efficient through single phase mixing. Lamanna et al. have also developed a model that estimates the time it takes for the droplet to become supercritical [8]. However, this model relies on data on evaporation coefficients at such conditions (near critical and high pressure), which are not available. To fill this gap, evaporation simulations are carried out at such conditions to extract the evaporation coefficients at the end.
In this work, such simulations have been performed with a particle-based statistical Enskog-Vlasov solver containing two species. A primary liquid species (argon) and a second species (neon) to apply the high pressure to the liquid. So far, only multi-species Enskog-Vlasov [5] solvers have been presented, which vary the strength of the intermolecular attraction potential of the different species [10, 6] but not their diameter, which is done in this work.

Numerical Modelling

The simulations are performed by an adapted Direct Simulation Monte Carlo [3] algorithm, which performs statistical particle simulations, where each particle represents a number of physical atoms. The behavior of the particles is simulated by statistical assumptions, which greatly reduces the computational effort compared to deterministic simulations such as Molecular Dynamics [7]. Statistical means that for different events (such as collisions) a probability is calculated and a random number determines whether the event takes place or not. In addition, random numbers determine the outcome of the event.
A schematic of the solver can be seen in Figure 1, which consists of several mostly decoupled steps, as movement of and collisions between the particles. At the beginning of each simulation the simulation is *initialized*, and the computational domain is populated with the simulation particles. Afterwards the time step loop starts, until the simulations ends. The first stage in this loop is the *field solver*, which determines the number density in each element and convolutes it with the derivative of the Sutherland potential to obtain the force onto the particles in every element. This force is used in the *particle movement* step to compute the new particle velocities and positions with a low storage explicit Runge-Kutta 3rd order. Subsequently, in the *boundary* step all particle paths are checked for intersections with boundaries and their conditions are applied to them.
In the *pairing* stage, the required number of particle pairs in each element for each species is generated: $N_{pairs} = \frac{1}{2} N P_{max}$, where N is the number of particles in the element and P_{max} is an estimate of the maximum collision probability based on the last time steps. For each pair,

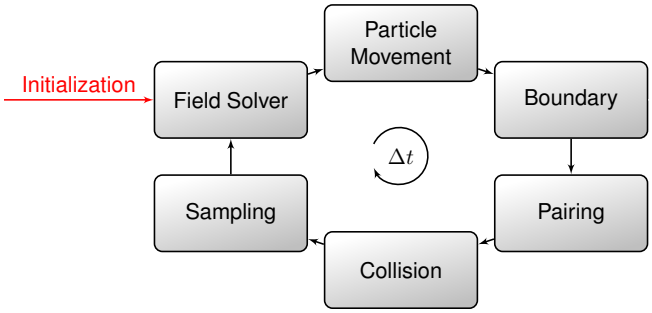

Figure 1. Schematic of the solver

the first particle is randomly selected and a random unit vector $\vec{k}$ is drawn. The second particle is the closest particle of the assigned species of the pair, located the mean diameter away from the first particle in the direction of $\vec{k}$. In the *collision* step, the equilibrium pair correlation function Y is evaluated, which incorporates the effects of the radial distribution function. Y is based on BMCSL equation of state [4] is evaluated for all pairs. This information is used to calculate the collision probability:

$$P = R\left(\left\langle \vec{c}_\mathrm{r} \cdot \vec{k} \right\rangle\right) \frac{4\pi d_{ij}^2}{\omega_k} Y\left(\vec{x} + \frac{d_i \vec{k}}{2}, i, j\right) n_{2,j} \Delta t \tag{1}$$

This collision probability is normalized by P_{max} and compared to a random number evenly distributed between zero and one. If the random number is lower, then the collision occurs and the particle velocities are updated by: $v_i' = v_i \pm 2\frac{m_i}{m_i+m_j} < \vec{c}_\mathrm{r} \cdot \vec{k} > \vec{k}$. In the final step *sampling* the particle properties are averaged to calculate the macroscopic moments as density n, bulk velocity u and temperature T.

Simulation Setup

The evaporation simulations were performed with an argon-neon mixture, where neon is in a supercritical state. To determine the molecular parameter, the strength of the attractive potential ϕ_d was fitted to critical temperature data. The molecular diameter for argon was fitted to equilibrium density simulations of SAFT-VR Mie [1, 2] simulations, while that of neon was fitted to pressure data [9]. The simulations were performed at three different temperature levels: $0.663T_{c,\mathrm{Ar}}$, $0.767T_{c,\mathrm{Ar}}$ and $0.9T_{c,\mathrm{Ar}}$. This gives the following parameters:

Table 1. Molecular properties of the simulations

	ϕ_d	$d(T = 0.663T_{c,\mathrm{Ar}})$	$d(T = 0.767T_{c,\mathrm{Ar}})$	$d(T = 0.9T_{c,\mathrm{Ar}})$
Ar	$2.759 \cdot 10^{-21}$ J	$3.332 \cdot 10^{-10}$ m	$3.227 \cdot 10^{-10}$ m	$3.142 \cdot 10^{-10}$ m
Ne	$8.136 \cdot 10^{-22}$ J	$2.590 \cdot 10^{-10}$ m	$2.566 \cdot 10^{-10}$ m	$2.549 \cdot 10^{-10}$ m

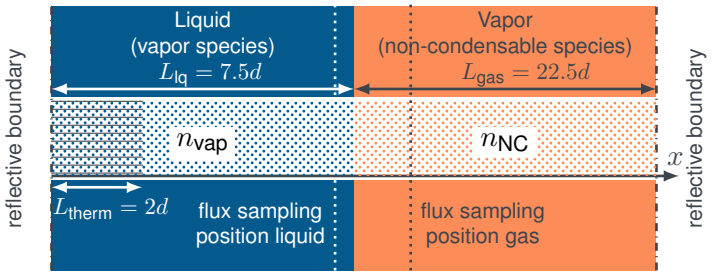

Figure 2. Initial condition of the simulations

The computational domain is an enclosed space of 30 cross-sectional diameter of argon and is depicted in Figure 2. A thermostat is required to maintain a stable temperature to counteract evaporation heat losses.

Results and Discussion

The results of the simulations are shown in Figure 3. It can be seen that at higher pressure and lower temperature more neon is dissolved in the liquid phase. In addition, more neon accumulates at the liquid-vapor interface. This accumulation can also be seen in other evaporation results [10]. With increasing pressure, the argon density in the vapor also increases.

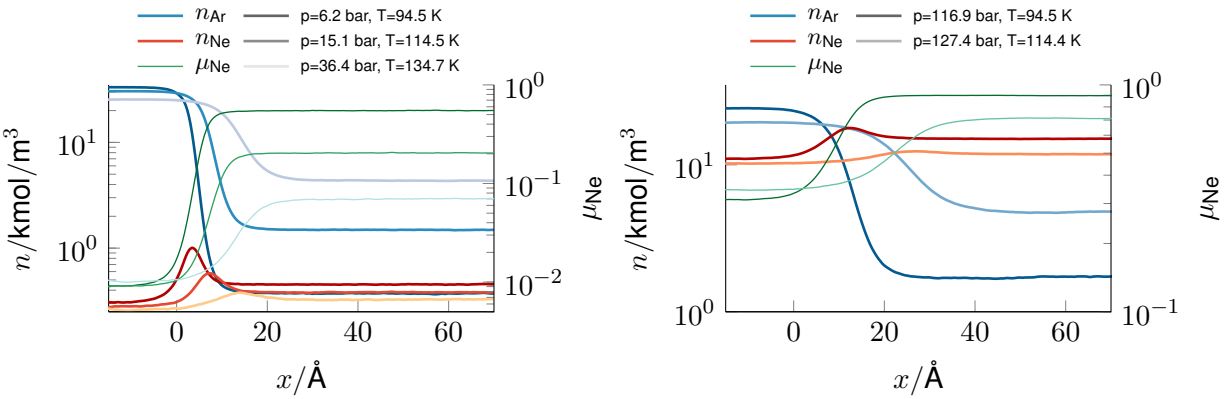

(a) Low pressure cases

(b) High pressure cases

Figure 3. number density profiles of the simulations

The mole fractions in the liquid and vapor regions were extracted and compared with the SAFT-VRQ Mie results [1, 2], which are shown in Figure 4. They show the same trend, but at higher pressures and temperatures the deviations are greater. This may be due to the use of different interaction potentials.

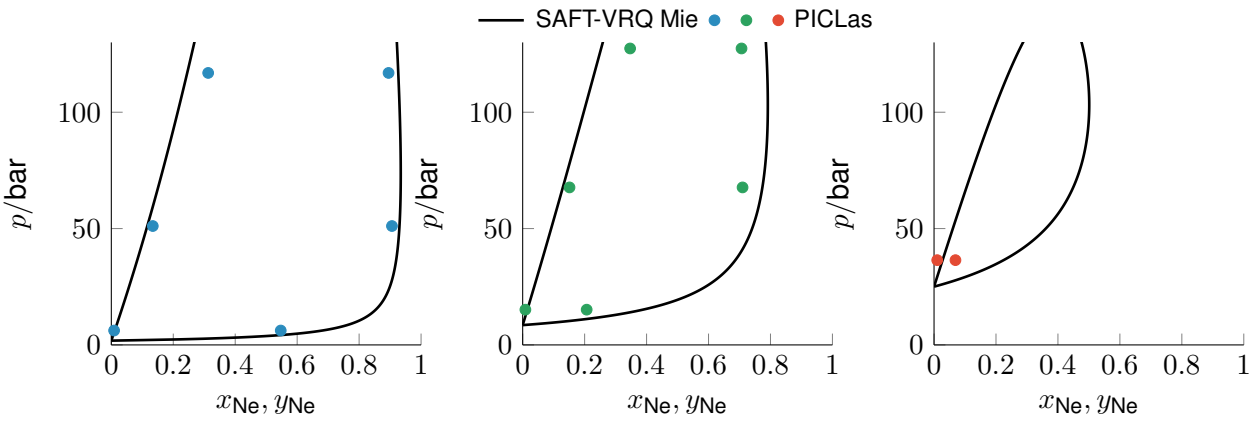

(a) $T/T_c = 0.633$

(b) $T/T_c = 0.767$

(c) $T/T_c = 0.900$

Figure 4. Enskog-Vlasov result compared to SAFT-VRQ Mie[1, 2]

Conclusion

This work briefly introduces a novel multi-species solver for the Enskog-Vlasov equation, which is able to simulate liquid vapor profiles of a binary mixture. The bulk vapour and liquid states are in good agreement with SAFT-VRQ Mie results.

The next steps are to perform further simulations of more application-like cases. From these simulations the evaporation coefficients can be sampled and fed into the Lamanna et al. model.

Nomenclature

Ar	argon [-]	t	time [s]
c_r	relative velocity [m/s]	T	temperature [K]
d	molecular diameter [m]	T_c	critical temperature [K]
i	Species [-]	$\vec{u}$	bulk velocity [m/s]
j	2nd Species [-]	$\vec{v}$	particle velocity [m/s]
$\vec{k}$	collision vector [-]	x	mole fraction in liquid [-]
m	molecular mass [kg]	y	mole fraction in vapor [-]
n	particle density [1/m^3]	$Y()$	equilibrium pair correlation function [-]
n_2	particle density in 2nd element [1/m^3]	Δt	time step length [s]
Ne	neon [-]	π	3.14159...[-]
p	pressure [bar]	ϕ_d	Sutherland potential strength at a distance of d [J]
P	collision probability [-]		
P_max	maximum collision probability [-]	ω_k	statistical particle weight [-]
		μ	mole fraction [-]

References

[1] A. Aasen, M. Hammer, Å. Ervik, E. A. Müller, and Ø. Wilhelmsen. *The Journal of Chemical Physics*, 151(6), 2019.

[2] A. Aasen, M. Hammer, E. A. Müller, and Ø. Wilhelmsen. *The Journal of Chemical Physics*, 152(7), 2020.

[3] G. A. Bird. *Molecular Gas Dynamics and Direct Simulation of Gas Flows*. Oxford Science Publications 42, 1994.

[4] T. Boublík. *The Journal of chemical physics*, 53(1):471–472, 1970.

[5] D. Enskog. *Kinetische Theorie der Wärmeleitung: Reibung und Selbst-diffusion in Gewissen verdichteten gasen und flüssigkeiten*. Almqvist & Wiksells boktryckeri-a.-b., 1922.

[6] A. Frezzotti, L. Gibelli, D. A. Lockerby, and J. E. Sprittles. *Physical Review Fluids*, 3(5):054001, 2018.

[7] A. Frezzotti, L. Gibelli, and S. Lorenzani. *Physics of Fluids*, 17(1), 2005.

[8] B. W. G. Lamanna, C. Steinhausen. On the role of transcritical evaporation in controlling the transition from two-phase to single-phase mixing. *32nd International Conference on Liquid Atomization and Spray Systems, Naples*, 2023.

[9] P. Linstrom and E. W.G. Mallard. *NIST Chemistry WebBook, NIST Standard Reference Database Number 69*. National Institute of Standards and Technology, 2024.

[10] K. Ohashi, K. Kobayashi, H. Fujii, and M. Watanabe. *Scientific Reports*, 10(1):8143, 2020.

Which wound dressing is better for rapid absorption of wound exudate?

Avick Sinha*[1,2], Anastasios Georgoulas[1,2], Matteo Santin[2]
[1]Centre for Regenerartive Medicine and Devices, University of Brighton, UK.
[2]Advanced Engineering Centre, University of Brighton, UK
*Corresponding author: A.Sinha@brighton.ac.uk

Introduction

Wound exudate plays a crucial role in the healing process, but its management is pivotal as excessive amounts can impede recovery. Wound dressings, which are essential for moisture control and infection prevention, come in thousands of varieties, making the selection of appropriate care challenging. These dressings, varying in their ability to absorb moisture and control exudate, must be effectively matched with wound needs to optimize healing [1]. However, the scarcity of clinical trials and quantitative data on dressing efficacy poses significant challenges, highlighting the need for further research to enhance wound care solutions. Porous wound dressings are involved in multiple roles, including absorption, gelling, retention, and moisture regulation. Regardless of the mechanism, it is crucial to understand that interactions with exudate can significantly alter the wound-dressing interface. As an initial step, quasi-sessile/sessile droplet experiments are essential to investigate the physics of exudate interactions with commercially available dressings.

Extensive research has explored droplet impacts on solid surfaces [2], liquid layers [2], and moving films [3], but little has been done on droplet impact on complex porous surfaces like wound dressings, involving both spreading and penetration. To our knowledge, no previous experimental or numerical studies have examined quasi-sessile droplet interactions with actual wound dressings. However, a few related related studies on liquid droplet absorption into porous materials are highlighted below.

Wallace and Yoshida [4] were among the first to investigate droplet impact on permeable surfaces, focusing on the spread factor—defined as the ratio of the droplet's maximum spread diameter to its initial diameter—on water-sensitive paper, particularly in relation to impact energy for pesticide spray applications. Delbos et al. [5] conducted a preliminary study on droplet imbibition in a single pore of a porous surface. They found that at low impact velocities (< 1 m/s) and with smaller pore sizes, hydrophobic pores prevent penetration, while hydrophilic pores allow the droplet to be absorbed. At higher impact velocities and with larger pores, part of the droplet enters the capillary, forming a slug. More recently, Andredaki et al. [6] numerically modeled the absorption of a quasi-sessile droplet by a single cylindrical pore, examining the effects of pore size, liquid viscosity, and droplet diameter. They concluded that the pore size and liquid properties primarily govern the absorption dynamics, with droplet diameter having minimal influence. Most previous experimental studies have overlooked very low velocities and quasi-sessile droplets. Additionally, only a few numerical studies have examined the simultaneous spreading and penetration of sessile droplets on single pores, which fail to capture the full complexity of droplet dynamics in wound dressings. Therefore, this study aims to enhance wound management by uncovering the complex physics of exudate-dressing interactions.

Materials and methods

This study evaluates seven commercially available wound dressings, classified by their material into three groups: Polyester (Kerramax, Melonin, and Atrauman), Cellulose (Aquacel, Kerracel, and NA-Ultra), and Alginate-based (Kaltostat). Using a ZEISS LSM 800 Confocal Microscope, a 2-D stack images were obtained, which were analysed to obtain the 3-D topology of the wound dressing fibre and fibre diameter and pore diameter. We employ Simulated Body Fluid (SBF), which replicates the ionic composition of human plasma, to examine the interactions between the dressings and the fluid, crucial for understanding their performance in wound healing scenarios. The dynamic viscosity and surface tension of SBF at 20^0 C is 0.968 ± 0.018 mPas and 70.73 ± 1.59 mN/m, respectively. An photograph of the experimental test rig is shown in Fig. 1. High-resolution, temporal (20 KhZ), and spatial analyses of droplet dynamics and imbibition characteristics on these dressings were conducted using a high-speed camera linked to a microscope. The spatial resolution after calibration was found to be 10 µm/pixel. Droplets of 2.13 mm ±0.04 mm in diameter (D), were generated by directing air from a small syringe linked to a larger syringe via a pneumatic tube. This airflow caused a droplet to form at the tip of the hypodermic needle. Subsequently, the droplet detached and descended towards the test section due to gravity, with a pre-contact velocity (U) of about 0.025

mm/s. All the captured images were thoroughly analyzed in MATLAB to investigate the dynamics of the droplet-wound dressing interactions.

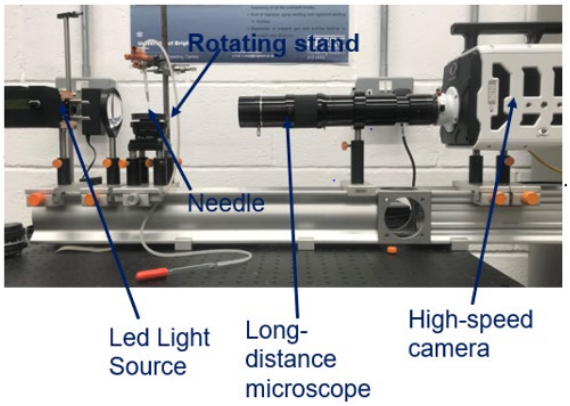

Figure 1. Experimental test rig showing the optical set-up.

Results and Discussion

Analyzing the images from the Confocal Microscope, it was observed that NA-Ultra has the largest pore diameter (see Fig. 2a), enhancing its potential for fluid absorption due to increased surface area. Additionally, NA-Ultra exhibited the largest fiber diameter (27 ± 4.5 µm), followed by Kaltostat (18 ± 3 µm), Kerramax (15 ± 3.5µm), and Melolin (10 ± 1µm). The fiber diameters of Melolin, Atrauman, Aquacel, and Kerracel were also found to be comparable within the margin of uncertainty.

Figure 1(b) shows the dynamic contact angle (θ_d) of three different wound dressings—Aquacel, Kerracel, and Kaltostat over non-dimensional time (T* = tD/U). At the beginning, all three dressings show a relatively high contact angle, suggesting they initially repel the fluid. This could be due to the intrinsic properties of the materials. Aquacel and Kerracel show a sharp decrease in contact angle early on. This indicates that the materials begin to absorb fluid more effectively as time progresses, reducing the contact angle as compared to Kaltostat.

Figure 1(c) depicts the penetration % of the droplet against T*. It can be observed that droplets penetrate faster in Kerracel as compared to Aquacel. This difference can be attributed to the higher porosity and pore diameter of Kerracel compared to Aquacel. The faster imbibition of cellulose-based dressing as compared to alginate-based dressing is because its glucose units are linked by glycosidic bonds with many hydroxyl (-OH) groups that form strong hydrogen bonds with water, enhancing its hydrophilicity. In contrast, alginate, a linear copolymer from seaweed with both hydroxyl and carboxylate groups, exhibits reduced hydrophilicity compared to cellulose.

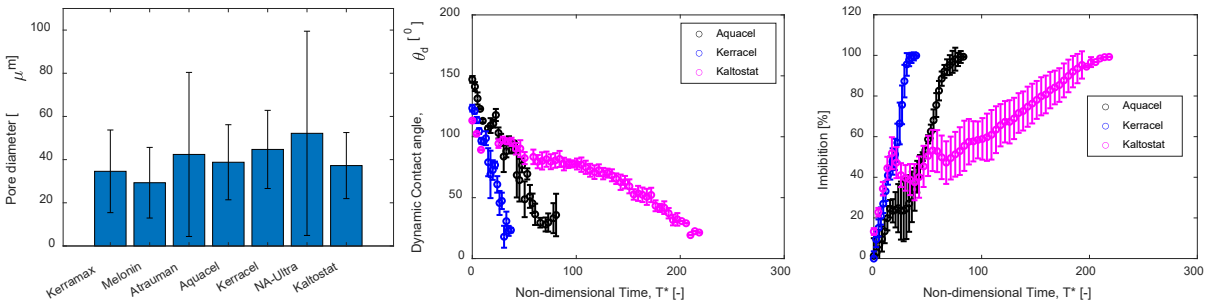

(a) (b) (c)

Figure 2. (a) Pore diameter of various wound dressings (b) Dynamic contact angle against non-dimensional time for three different wound dressings (c) Imbibition against non-dimensional time for three different wound dressings.

Conclusion

The complete penetration of droplets into the wound dressing is driven by the combined effects of hydrodynamic focusing and capillary forces, improving the dressing's ability to manage wound exudate effectively. Moreover, cellulose-based dressings such as Kerracel and Aquacel absorb faster compared to alginate-based wound dressings (Kaltostat).

From a clinical point of view, wound dressings that quickly reduce contact angles are preferable for managing wounds with high exudate levels, swiftly drawing moisture away from the wound site. Specifically, cellulose-based dressings are recommended over alginate-based for their superior absorption capabilities in high-exudate scenarios. A parallel in-house study that has been conducted under the umbrella of the same research project and it was found that exudates behave as shear-thinning fluids, thus the droplet dynamics will be different as compared to the present study. Future research will incorporate shear-thinning fluids and conducting experiments in microchannels to explore exudate behaviour within pores.

References

[1] Forss, J.R., Does exudate viscosity affect its rate of absorption into wound dressings? *Journal of Wound Care*, *31*(3), 236-242 (2022).

[2] Yarin, A.L., Drop impact dynamics: Splashing, spreading, receding, bouncing. . . , Annu. Rev. Fluid Mech. 38 159–192 (2006).

[3] Sinha, A., Ramakrishnan, V., Johnson, K., Droplet impact on a curved moving liquid film, in: Turbo Expo: Power for Land, Sea, and Air, Vol. 86106, American Society of Mechanical Engineers, p. V10BT31A003 (2022).

[4] Wallace, K., Yoshida, K., Determination of dynamic spread factor of water droplets impacting on water-sensitive paper surfaces, Journal of Colloid and Interface Science 63 (1) 164–165 (1978).

[5] Delbos, A., Lorenceau, E., Pitois, O., Forced impregnation of a capillary tube with drop impact, Journal of colloid and interface science 341 (1) 171–177 (2010).

[6] Andredaki, M., Georgoulas, A., Marengo, M., Numerical investigation of quasi-sessile droplet absorption into wound dressing capillaries, Physics of Fluids 32 (9) (2020).

Simulation framework for drop impacts on structured surfaces using PLIC-based contact line modeling

J. Wurst*[1], K. Schulte[1]
[1]Institute for Aerospace Thermodynamics, University of Stuttgart, Germany
*Corresponding author: jonathan.wurst@itlr.uni-stuttgart.de

Introduction

Developments in the field of surface technology promise custom-tailored surface structuring and require an understanding of the interaction with fluids. Our aim is to investigate drop impacts onto regularly structured surfaces with highly resolved direct numerical simulations. We therefore present in this paper a simulation framework with appropriate methods to capture the complex flow dynamics appearing inside the grooves. Free Surface 3D [2], our in-house multiphase flow solver, is updated accordingly and validated with several test cases. Included in the validation are an analytic test case as well as an experimental comparison that demonstrate the abilities of the framework.

Material and methods

The multiphase flow solver Free Surface 3D is based on the finite volume method and uses a Cartesian staggered grid. The Volume-of-Fluid (VoF) method [4] is applied together with the piecewise linear interface calculation (PLIC) [10] for tracking the phase distributions. The code adaption included a dynamic contact angle model and the reconstruction of the interface as well as imposing the correct surface tension at the solid boundary and are explained in the following sections.

Dynamic contact angle model - The angle at which a free surface is in contact with a solid substrate is called the equilibrium or static contact angle θ_{st} and can in theory be expressed by the famous Young equation. On the micro-scale still the capillary forces dominate for a moving contact line, while on the macro-scale viscous and inertial forces compete and cause the interface to bend. Due to the different scales, refining the grid size around the contact line leads to mesh-dependent solutions. Following the idea of Afkhami et al. [1], Cox' theory is used to apply a mesh-dependent contact angle. A polynomial approximation for fluids with a high viscosity ratio is Mathieu's model [5]

$$\theta_{dyn} = g^{-1}\left(g(\theta_{st}) + Ca\ln\left(\frac{r_0}{\lambda}\right)\right), \tag{1}$$

$$g(\theta) = \frac{1}{9}\theta^3 - 0.00183985\theta^{4.5} + 1.845829\cdot 10^{-6}\theta^{12.258487}, \tag{2}$$

$$g^{-1}(\theta) = (9\theta)^{1/3} + 0.0727387\theta - 0.0515388\theta^2 + 0.0034136\theta^3, \tag{3}$$

with the outer length scale $r_0 = \Delta z$, on which the contact angle is applied and thus set to the grid spacing Δz, and the slip length λ, lying in the order of 10^{-9}m. The application of this formulation showed good grid convergence for a spreading drop test case and was therefore used in our simulations.

Reconstruction of the interface - In cells neighboring the rigid wall, a full symmetric stencil is not available and the orientation can usually not be determined with a standard scheme. Hence, a combination of the approaches by Patel et al. [7] and Pathak and Raessi [8] is applied, as proposed by Potyka and Schulte [9]. The basic idea behind this is the minimization of an objective function that takes into account how well the orientation approximates also adjacent cells.

Surface tension at solid boundary - The method of Sussman [11] provides ghost values of the volume fraction to apply the numerical scheme also at the boundary. This approach is especially useful to switch between surface tension models and is also applicable to immersed

$$\boldsymbol{u}_{ext} = \frac{\boldsymbol{n}_{wall} + \cot(\theta)\boldsymbol{n}_2}{|\boldsymbol{n}_{wall} + \cot(\theta)\boldsymbol{n}_2|}, \tag{4}$$

$$\boldsymbol{n}_2 = -\frac{\boldsymbol{n}_1 \times \boldsymbol{n}_{wall}}{|\boldsymbol{n}_1 \times \boldsymbol{n}_{wall}|}, \tag{5}$$

$$\boldsymbol{n}_1 = -\frac{\boldsymbol{n}_f \times \boldsymbol{n}_{wall}}{|\boldsymbol{n}_f \times \boldsymbol{n}_{wall}|}. \tag{6}$$

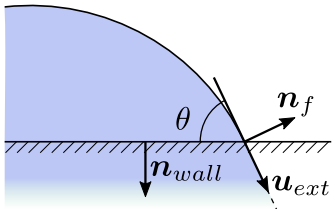

Figure 1. Sketch of Sussman's method. The extension velocity $\boldsymbol{u}_{ext}$ is constructed to transport the liquid according to the contact angle θ into the wall.

boundaries. Sussman's basic idea is to artificially transport the liquid phase into the ghost cells. An extension velocity $\boldsymbol{u}_{ext}$ is calculated via Eq. (4) that points parallel to the interface into the wall, see Fig. 1. After constructing $\boldsymbol{u}_{ext}$, several steps of the advection scheme are performed with a time step of $\Delta t = 0.5\Delta z|\boldsymbol{u}_{ext}|^{-1}$, which proved to be a robust choice for a wide range of contact angles tested. This approach is also applied for situations with a structured surface. The solid for structured surfaces is hereby represented by an additional volume fraction f_3, but neglected during this artificial fluid transport. The procedure can then be applied straight forward, only the wall normal $\boldsymbol{n}_{wall}$ has to be computed locally in the computational cells, depending on the position along the structured surface.

Results and Discussion

For the validation, an analytic test case as well as an experimental drop impact are simulated. A square capillary serves as a static test that can be examined also analytically and P. Palmetshofer [6] provided experimental data to validate the simulation also with an experiment. Both cases are presented in the following sections.

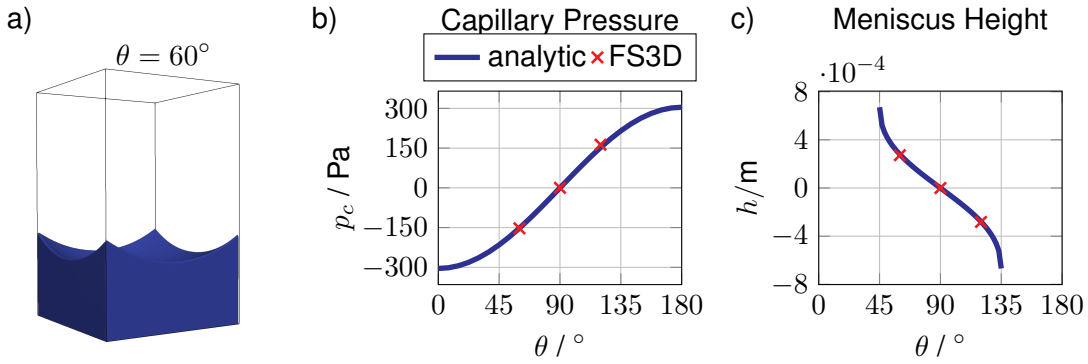

Figure 2. Results of the square capillary test case. a): Meniscus contour for a contact angle of $\theta = 60°$. b): Capillary pressure from analytic solution Eq. (7) and FS3D. c): Meniscus height from analytic solution Eq. (8) and FS3D.

Square capillary - The shape of a meniscus in a capillary channel in the absence of gravity can be described analytically. A similar situation can arise for the fluid flow between pillars or grooves of a structured surface after a drop impact. The capillary pressure p_c and the meniscus height h as a function of the channel width a and the contact angle are given as [3]

$$p_c = \frac{4\sigma\cos(\theta)}{a}, \tag{7}$$

$$h = \frac{a}{2\cos(\theta)}\left[1 - \sqrt{1 - 2\cos(\theta)^2}\right]. \tag{8}$$

Three different configurations with contact angles of $\theta = 60°, 90°, 120°$ were simulated until a static solution was reached. The final contour of the smallest contact angle is displayed in Fig. 2a). A comparison with the analytic solution of the capillary pressure and meniscus height can be seen in Fig. 2b)-c). The capillary pressure for $\theta = 120°$ shows the largest deviation of 7% while all other results are below 3%. This clearly demonstrates a valid implementation for a static case.

Drop impact on structures - As a second validation case, an experiment of an isopropanol droplet impact onto a structured surface is simulated. The structures are pillars with the same height, width and separation of $d_s = 0.2\,\mathrm{mm}$. The initial velocity and diameter was $u_0 = 1.62\,\mathrm{m\,s^{-1}}$ and $D_0 = 1.88\,\mathrm{mm}$, respectively, corresponding to a Weber number $We = 180$ and Reynolds number $Re = 1160$. The substrate is superhydrophilic with a contact angle between $\theta = 5^\circ - 10^\circ$, in the simulation the static angle was set to $\theta = 10^\circ$. In Fig. 3, experimental images are shown together with snapshots of the simulation from a side-view and a viewpoint from above. The qualitative agreement in these pictures is very good, the imbibition process is captured correctly as well as the resulting diamond-shape.

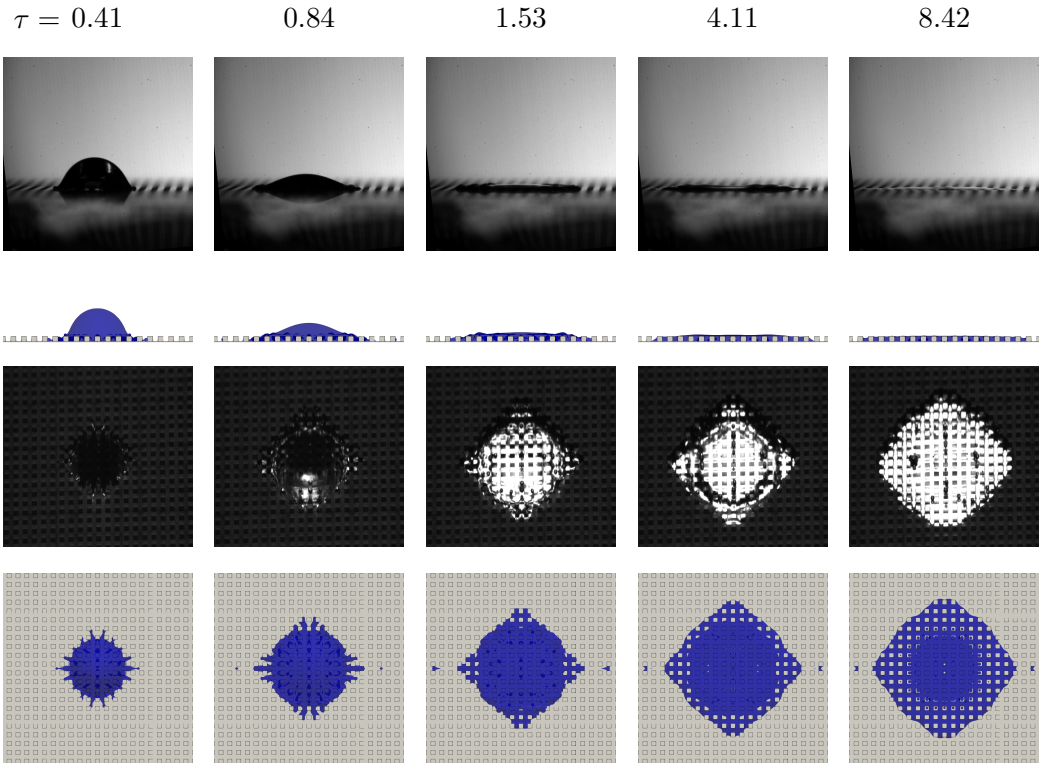

Figure 3. Snapshots of the simulation of an isopropanol drop impact ($\mathrm{We} = 180, \mathrm{Re} = 1160$) on pillars of size $d_s = 0.2\,\mathrm{mm}$ for different non-dimensional times in comparison with the experiment.

Additionally, in Fig. 4 the spreading factors in axial (0°) and diagonal (45°) direction with respect to the pillar orientation are displayed as a function of the dimensionless time $\tau = tu_0/D_0$. The graphs agree well during the entire process and especially at later times, where a capillary driven motion takes place. The deviation between experiment and simulation is at all times below 10%. This further confirms the correctness of our implementation.

Conclusion

The solver FS3D was adapted to be able to simulate wetting phenomena on structured surfaces. The implementation was validated with analytic test case of a square capillary and an experiment of droplet impact on a regularly structured surface. The simulation exhibits a maximum error of 7% to the analytic solution while for the experimental comparison the deviation was determined to be less than 10%. We therefore conclude that the presented framework is able to predict drop impacts on structured surfaces to an accurate degree.

Nomenclature

a	channel width [m]	$\boldsymbol{u}_{ext}$	extension velocity [m/s]
Ca	Capillary number [-]	Δt	time step [s]
d_s	structure size [m]	Δz	grid spacing [m]

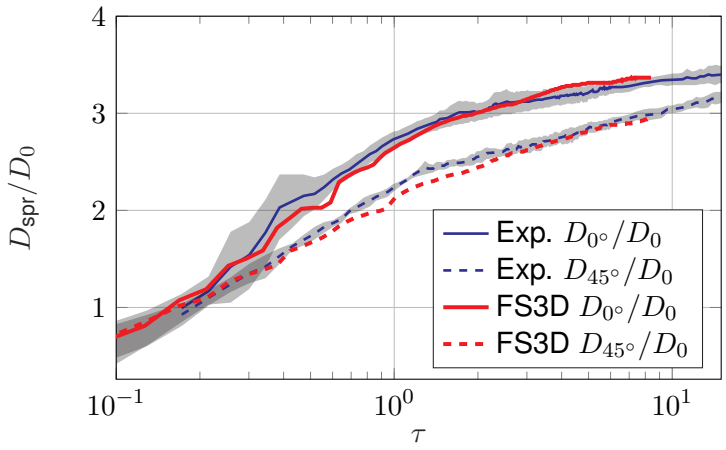

Figure 4. Axial and diagonal spreading factors over time of FS3D and the experiment. The darker areas indicate the standard deviation of the experiment.

f	phase fraction [-]	θ	contact angle [°]
h	meniscus height [m]	λ	slip length [m]
$\boldsymbol{n}$	normal vector [-]	μ	dynamic viscosity [Pa s]
p_c	capillary pressure [Pa]	σ	surface tension [N/m]
r_0	apparent length [m]	τ	dimensionless time [-]
u_{cl}	contact line velocity [m/s]		

References

[1] S. Afkhami, S. Zaleski, and M. Bussmann. A mesh-dependent model for applying dynamic contact angles to vof simulations. *Journal of Computational Physics*, 228(15):5370–5389, 2009.

[2] K. Eisenschmidt, M. Ertl, H. Gomaa, C. Kieffer-Roth, C. Meister, P. Rauschenberger, M. Reitzle, K. Schlottke, and B. Weigand. Direct numerical simulations for multiphase flows: An overview of the multiphase code FS3D. *Journal of Applied Mathematics and Computation*, 272(2):508–517, 2016.

[3] J. Feng and J. P. Rothstein. Simulations of novel nanostructures formed by capillary effects in lithography. *Journal of Colloid and Interface Science*, 354(1):386–395, 2011.

[4] C. W. Hirt and B. D. Nichols. Volume of fluid (VOF) method for the dynamics of free boundaries. *Journal of Computational Physics*, 39(1):201–225, Jan. 1981.

[5] B. Mathieu. *Etudes physique, expérimentale et numérique des mécanismes de base intervenant dans les écoulements diphasiques en micro-fluidique*. PhD thesis, Université de Provence, 2003.

[6] P. Palmetshofer and B. Weigand. Splashing modes in droplet impacts onto sub-millimeter microstructures. In *Proceedings of the DIPSI Workshop 2024: Droplet Impact Phenomena & Spray Investigations*. Università degli studi di Bergamo, 2024.

[7] H. Patel, S. Das, J. Kuipers, J. Padding, and E. Peters. A coupled volume of fluid and immersed boundary method for simulating 3d multiphase flows with contact line dynamics in complex geometries. *Chemical Engineering Science*, 166:28–41, 2017.

[8] A. Pathak and M. Raessi. A three-dimensional volume-of-fluid method for reconstructing and advecting three-material interfaces forming contact lines. *Journal of Computational Physics*, 307:550–573, 2016.

[9] J. Potyka and K. Schulte. A volume of fluid method for three dimensional direct numerical simulations of immiscible droplet collisions. *International Journal of Multiphase Flow*, 170:104654, 2024.

[10] W. J. Rider and D. B. Kothe. Reconstructing volume tracking. *Journal of Computational Physics*, 141(2):112–152, Apr. 1998.

[11] M. Sussman. *An adaptive mesh algorithm for free surface flows in general geometries*. Chapman and Hall/CRC Boca Raton, FL, USA, 2001.

DNS of droplet impact onto heated surfaces

R. Saha*, B. Weigand
Institute of Aerospace Thermodynamics, University of Stuttgart, Germany,
*Corresponding author: rishav.saha@itlr.uni-stuttgart.de

Introduction

Droplet impact onto heated surfaces is a widespread process, which is encountered in many existing cooling technologies [1] used in industrial applications. These cooling technologies often involve multiple droplets, such as in sprays, but understanding their behaviour is complex. Therefore, we first need to study the impact dynamics and heat transfer mechanism of a single droplet impact onto a homogeneously heated substrate. This single droplet impact process can be influenced by numerous factors, including droplet parameters, liquid properties, surrounding gas parameters, and surface characteristics [2]. In this study, the impact dynamics of a water droplet impacting onto a highly conducting material is simulated. This work focuses on the temperature changes of the droplet's liquid during its spreading process within the film evaporation regime.

When a droplet at room temperature comes into contact with a heated surface, the liquid absorbs heat from the surface because of the temperature difference. This heat absorption results in a cooling effect on the heated surface, which is an advantageous strategy widely used in industrial applications [1]. Depending on the impact velocity, a droplet typically splashes, bounces or spreads onto the surface. Maximum heat transfer to the liquid is achieved when a droplet sticks to the surface for a longer period of time. However, the solid-liquid contact time and area is relatively higher for spreading droplets than droplet splashing and bouncing [3]. Therefore, investigating heat transfer during the spreading process is essential. Here, a water droplet impact onto an iso-thermally heated surface with a static contact angle of 90 deg. is simulated, from just before droplet-wall contact until the recoiling stage.

Methods

Direct Numerical Simulation (DNS) is conducted using the in-house multiphase flow solver code Free Surface 3D [4] (FS3D) running on a supercomputer of the High-Performance Computing Center Stuttgart (HLRS), HPE Apollo Hawk platform. The study is conducted both from the hydrodynamic and heat transfer perspective in a Computational Fluid Dynamic (CFD) framework. The incompressible Navier-Stokes equations are solved using the Finite-Volume method, where the interface is captured using the Volume of fluid [5] (VOF) method in a Cartesian grid. Separate temperature fields are solved for both phases [6]. The continuum surface force [7] (CSF) model is used, while the interface reconstruction is performed using the piecewise linear interface calculation (PLIC) method.

A quarter of a droplet, with an initial diameter of D_0 = 2 mm and an initial impact velocity of V_0 = 3 m/s, is initialised in a cubic domain of size $2D_0$. The surrounding ambient of the droplet is at 1 atmospheric pressure, and the initial temperature is 298 K. The gravitational force g acts in the downward direction. Continuous boundary conditions were applied to the far faces of the domain except for symmetric planes and the bottom surface. The bottom surface is assumed to be a highly conductive substrate, therefore, an isothermal boundary condition is enforced at a temperature of 363 K, below the boiling point of water. Evaporation is ignored as the time scale of evaporation is large compared to the spreading time scale. In figure 1, a schematic 2D diagram of the computational domain and a 3D visualization of the computational domain is shown.

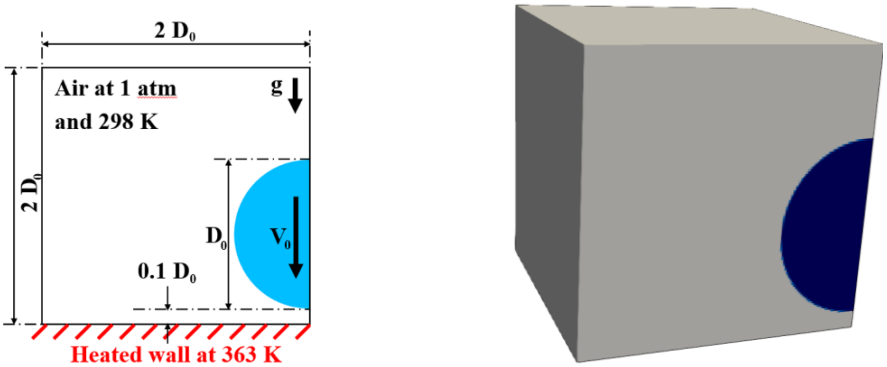

Figure 1. (Left) Schematic 2D diagram of the computational domain with domain configuration at the initial time. (Right) 3D visualization of the computational domain showing a quarter of the droplet.

Results and Discussion

The DNS were conducted for a simulation time of 3 ms, which corresponds to a dimensionless time of $\tau = 4.5$, where

$$\tau = (t\, V_0)/\, D_0 \qquad (1)$$

A line probe *L* is placed at the middle of the domain to record the temperature distribution along the z-axis at different time instances, for the gas liquid system, shown in figure 2. Grid sizes were increased systematically by a factor of two, from 256 to 1024 in each direction of the cubic domain, which resulted in a systematic increase in the total number of cells from two million to one billion. Hence, the number of cells per initial drop diameter was varied from 128 cells to 512 cells. To record the liquid temperature profile at the probe just after 1 dimensionless time, solution at $\tau = 1.25$ is used. Solution with grids 512^3 show convergences in the liquid temperature, shown in figure 2. It is observed that an increase of a maximum of 5 K is recorded in the liquid temperature until a maximum height of 40 µm above the surface. This change can be considered negligible for influencing the temperature-dependent material properties of water, such as viscosity, density, and surface tension.

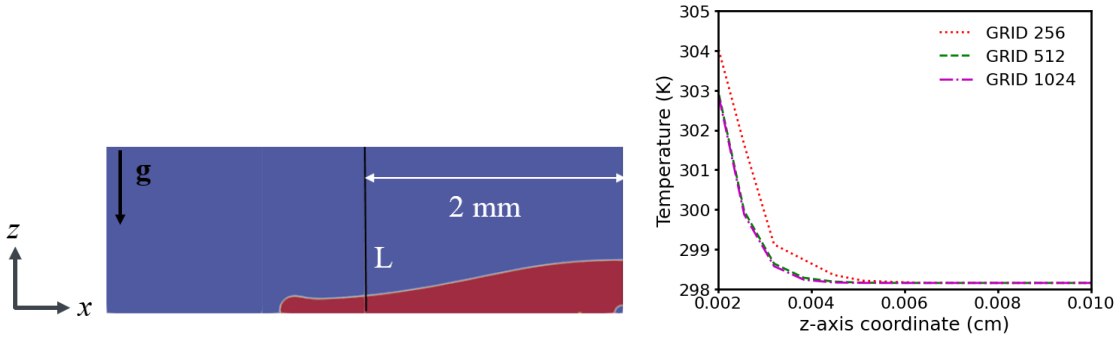

Figure 2. (Left) Location of the line probe *L* is shown at $\tau = 1.25$. (Right) Temperature profile for solution with grids 256^3, 512^3 and 1024^3, along the line probe *L* at $\tau = 1.25$.

Conclusion

A DNS study of the spreading process of a small water droplet impacting onto a heated surface is performed. A grid resolution of 512^3 was found to be sufficient enough to adequately resolve the impact dynamics and heat transfer in the liquid for the droplet considered in the present study. A line probe is utilized to record the increase in liquid temperature during spreading. As the droplet spreads, it forms a rim at the edge and attains maximum diameter, which is followed by a recoiling stage. It is observed that during spreading, only a very thin portion of the liquid film is heated, indicating that the heat conduction timescale is less than the spreading timescale for the water. The temperature independent material property assumption still holds, as the thermodynamic and fluid properties of water has a negligible change with a temperature difference of 5 K.

Future works

In this work, simplest configurations are used for the study of droplet impact onto a heated surface. However, the heat transfer mechanism for the process is very complex. To understand this, we need to consider different liquids such as, Heptane, Ethanol, Acetone and other engineering fluids, which has a lower specific heat compared to water, and volatile in nature. So that, the conduction timescale and the spreading timescale overlap and both the effects can be observed in the simulation, to have a greater influence in spreading and heat transfer.

Acknowledgments

We appreciate the financial support of this work by the Deutsche Forschungsgemeinschaft (DFG) in the framework of the International Research Training Group “Droplet Interaction Technologies” (GRK 2160/2: DROPIT) under project number 270852890. Furthermore, we would like to thank the *High-Performance Computing Center Stuttgart* (HLRS) for providing computation time on the HPE Apollo Hawk platform under Grant Number FS3D/11143.

References

[1] Jia, W., Qiu, H.H.: Experimental investigation of droplet dynamics and heat transfer in spray cooling. Exp. Therm. Fluid Sci. 27(7), 829–838 (2003)
[2] Liang, G., Mudawar, I.: Review of drop impact on heated walls. Int. J. Heat Mass Transfer. 106, 103–126 (2017)

[3] Josserand, C., Thoroddsen, S.T.: Drop impact on a solid surface. Annu. Rev. Fluid Mech. 48, 365–391 (2016)
[4] Eisenschmidt, K., Ertl, M., Gomaa, H., Kieffer-Roth, C., Meister, C., Rauschenberger, P., Reitzle, M., Schlottke, K., Weigand, B.: Direct numerical simulations for multiphase flows: An overview of the multiphase code FS3D. Appl. Math. Comput. 272, 508–517 (2016)
[5] Hirt, C.W., Nichols, B.D.: Volume of fluid (vof) method for the dynamics of free boundaries. J. Comput. Phys. 39(1), 201–225 (1981)
[6] Schlottke, J., Dulger, E., Weigand, B.: A vof-based 3d numerical investigation of evaporating, deformed droplets. Prog. Comput. Fluid Dyn. 9(6-7), 426–435 (2009)
[7] Brackbill, J.U., Kothe, D.B., Zemach, C.: A continuum method for modeling surface tension. J. Comput. Phys. 100(2), 335–354 (1992

Heating and evaporation of sessile droplets: new models of the processes

S.S. Sazhin*[1,2,3], D.V. Antonov[3], E.M. Starinskaya[2,4], V.V. Terekhov[2], S.V. Starinskiy[2,4,5]

[1]Advanced Engineering Centre, School of Architecture, Technology and Engineering, University of Brighton, Brighton, BN2 4GJ, United Kingdom

[2]Kutateladze Institute of Thermophysics, Siberian Branch of the Russian Academy of Sciences, 1 Lavrentiev Avenue, Novosibirsk 630090, Russian Federation

[3]National Research Tomsk Polytechnic University, 30, Lenin Avenue, Tomsk, 634050, Russian Federation

[4]Novosibirsk State University, Pirogova Str. 2, 630090 Novosibirsk, Russian Federation

[5]Theoretical and Physical Chemistry Institute, National Hellenic Research Foundation, 11635 Athens, Greece

*Corresponding author: S.Sazhin@brighton.ac.uk

Introduction

The importance of investigation of heating and evaporation of sessile droplets in various applications is well known and has been widely discussed in the literature [4, 6]. It has been demonstrated that droplet evaporation characteristics depend on many factors, including the humidity and temperature of ambient air, the physical properties of liquids, wettability and surface roughness (e.g. [5]). A number of models of the phenomena have been developed, starting with simple one-dimensional analytical-numerical models [1] and ending with the two-dimensional analytical model [7], and fully numerical models (e.g. [3, 2]). This abstract is focused on a brief analysis of the approaches to modelling these processes in sessile droplets described in [1, 3, 2].

Material and methods

A two-dimensional (2D) axisymmetric geometry, used in the modelling, is shown in Figure 1. 2D formulation of the problem was justified by the observed axial symmetry of the processes under consideration. In the advanced formulation of this approach, transport equations were solved numerically using COMSOL Multiphysics (Version 6.2) with the modules Nonisothermal Flow, Two-Phase Laminar Flow, Heat Transfer in Solids and Fluids, Transport of Diluted Species, and Moving Mesh.

The simple 2D model assumed that droplets retain their truncated spherical shapes during the evaporation process. In this model, the 2D version of the heat transfer equation was solved numerically using the above-mentioned COMSOL code. Droplet deformation, temperature gradients along the droplet surface, and the Marangoni effect were not considered in this model [3].

The one-dimensional (1D) model used the analytical solution to the spherically symmetric heat transfer equation with the source term which was implemented into the numerical code and used at each time step of the calculations. It was assumed that heat supplied by conduction from the plate to the droplet is homogeneously and instantaneously distributed throughout the whole droplet volume. It was also assumed that the droplet retains its spherical shape during the evaporation process. The effects of temperature gradient along the droplet surface were ignored.

Results and Discussion

The results of experimental and theoretical investigation of the dynamics, heating and evaporation of sessile water-ethanol droplets on a heated aluminum-magnesium alloy AMg6 plate are presented following [2]. Time dependencies of the diameter of the contact area, dynamic contact angle, and relative droplet volume at three temperatures of the plate are described.

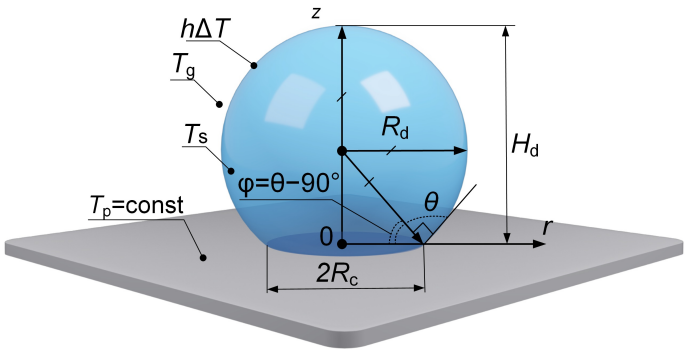

Figure 1. A two-dimensional axisymmetric geometry used for the analysis of heat/mass transfer during evaporation/heating of a sessile droplet. Copyright Elsevier (2024).

Three modes of droplet evaporation were identified: spreading (contact radius (R_c) increases with time), pinning (R_c oscillates about an average value), and mixed mode (R_c decreases with time). It is shown that during the oscillation of R_c in the pinning mode the value of $|\mathrm{d}R_c/\mathrm{d}t|$ does not exceed 0.004 mm/s. This value of $|\mathrm{d}R_c/\mathrm{d}t|$ was used as the criterion for transition between spreading, pinning, and mixed modes [2]. For the spreading mode, $\mathrm{d}R_c/\mathrm{d}t \geq 0.004$ mm/s; for the pinning mode, $|\mathrm{d}R_c/\mathrm{d}t| < 0.004$ mm/s; and for the mixed mode, $\mathrm{d}R_c/\mathrm{d}t < -0.004$ mm/s.
The predictions of all three models were validated using in-house experimental data obtained from studies of sessile droplets of distilled water with initial volumes of 5.2, 3.2, and 2.2 μl, at an ambient temperature of 298.15 K, and at atmospheric pressure. The observed time dependencies of relative droplet volume for a wide range of ambient air humidities and plate temperatures are shown to agree with those predicted by COMSOL, but differ considerably from the predictions of the 1D model [3]. The silicon surface was treated with nanosecond laser radiation and then functionalised with a superhydrophobic fluoropolymer coating that was about tens of nanometers thick.
It was shown in [3] that the simple 2D and 1D models correctly predict the initial rapid decrease in T_s followed by its gradual increase, in agreement with the experimental data. The values of T_s predicted by these models at the very initial stages of droplet heating/cooling and evaporation are close to those predicted by the advanced 2D model and experimental data.

Conclusion

Recently developed advanced and simple two-dimensional (2D) models of sessile droplet heating/cooling and evaporation are described. In contrast to the earlier developed one-dimensional (1D) model both new 2D models consider the spatial distribution of heat supplied by the surface. The advanced 2D model is based on the numerical solution to the equations of conservation of mass, momentum, vapour mass fraction, and energy with standard boundary and initial conditions, using COMSOL Multiphysics code. Simple 2D and 1D models assume that droplets retain their truncated spherical shapes during the evaporation process. In the 1D model, the analytical solution to the 1D heat conduction equation inside the droplet is implemented into a numerical code.
The time dependences of the droplet average surface temperature, predicted by the advanced 2D model, are demonstrated to be close to those observed experimentally. The 1D and simple 2D models can correctly predict the initial rapid decrease in droplet average surface temperature followed by its gradual increase, in agreement with experimental data.
The results of investigation of dynamics, heating and evaporation of sessile water-ethanol droplets on a heated aluminium-magnesium alloy AMg6 plate are described. Three modes of droplet evaporation are identified following [2]: spreading (contact radius increases with time), pinning when this radius oscillates about an average value, and mixed mode when it decreases with time. The criteria for transition between these modes are described, following [2], based on the maximal amplitude of oscillations of this radius in the pinning mode. The observed time

dependencies of relative droplet volume for a wide range of ambient air humidities and plate temperatures agree with those predicted by COMSOL, but differ from those predicted by the 1D model.

Nomenclature

h	convection heat transfer coefficient [W/m^2 K]
H	height of the droplet [m]
$r,\ z$	axes of the cylindrical coordinate system [m]
R_c	radius of the contact area [m]
R_d	droplet radius [m]
t	time [s]
T	temperature [K]

Greek symbols

$\varphi,\ \theta$	angles shown in Figure 1 [rad]

Subscripts

c	contact area
d	droplet
g	ambient gas
p	plate
s	droplet surface
0	initial

Acknowledgments
Financial support received the Russian Science Foundation (Grant 23-73-30004) and Ministry of Science and Higher Education of the Russian Federation (Grant 075-15-2024-620) is gratefully acknowledged. The research presented in the paper was initiated during work on a project supported by the Royal Society (UK) (Grant no. IEC 192007).

References

[1] D. V. Antonov, R. M. Fedorenko, P. A. Strizhak, and S. S. Sazhin. *International Journal of Heat and Mass Transfer*, 201:123568, 2023.
[2] D. V. Antonov, A. G. Islamova, P. A. Strizhak, and S. S. Sazhin. *International Journal of Heat and Mass Transfer*, 232:125948, 2024.
[3] D. V. Antonov, E. M. Starinskaya, S. V. Starinskiy, N. B. Miskiv, V. V. Terekhov, P. A. Strizhak, and S. S. Sazhin. *Langmuir*, 40(5):2656–2663, 2024.
[4] D. Brutin and V. Starov. *Chem. Soc. Rev.*, 47:558–585, 2018.
[5] Y. Fukatani, D. Orejon, Y. Kita, Y. Takata, J. Kim, and K. Sefiane. *Phys. Rev. E*, 93:1–16, 2016.
[6] G. V. Kuznetsov, F. D. V., E. G. Orlova, S. Y. Misyura, V. S. Morozov, and A. G. Islamova. *International Journal of Heat and Mass Transfer*, 126:161–168, 2018.
[7] S. Tonini and G. E. Cossali. *Phys. Fluids*, 36:027131, 2024.

NMF - Based Analysis of Droplet Wall-Film Interactions

Daniel Klötzl* and Daniel Weiskopf
Visualization Research Center (VISUS), University of Stuttgart, Stuttgart, Germany
*Corresponding author: daniel.kloetzl@visus.uni-stuttgart.de

Keywords
Nonnegative Matrix Factorization, Droplet Wall-Film Interactions, Visualization

Introduction

The automated and explainable characterization of droplet wall-film impact outcomes and secondary phenomena is of great interest to many modern technological applications and natural processes. We use nonnegative matrix factorization (NMF) to decompose ensembles of experiments of droplets impacting a thin liquid layer. In prior work, nonnegative matrix factorization was used to identify areas of interest in mobile eye-tracking recordings in an unsupervised way [1]. Here, a general approach to applying NMF for the analysis of multiple video data together with suitable visualization techniques is introduced that utilize the interpretable NMF decomposition (via their matrix dimensions):

$$\mathbf{X} \simeq \mathbf{WH}, \quad \mathbf{X} \in \mathbb{R}^{🌐 \times ⏱}, \mathbf{W} \in \mathbb{R}^{🌐 \times k}, \mathbf{H} \in \mathbb{R}^{k \times ⏱}.$$

In fact, NMF decomposes the data into user-defined $\boldsymbol{k}$ spatiotemporal components representing different phenomena throughout the recordings. As a result, each component offers a spatial representation and a temporal indicator that shows the occurrence within the recordings. The number of NMF components enables the user to either decompose the recordings into large-scale phenomena (low k) or small-scale outliers (high k).
We demonstrate the usefulness of our visual analysis with a challenging ensemble of monochrome camera recordings for different fluids, droplet sizes, zoom, and illumination.

Investigated dataset: The droplet splash dataset by Geppert [2] is given as an ensemble of monochrome camera images of a single droplet impacting a thin liquid layer. The experiments include different liquids for both droplets and wall-films and differ in impact velocities and droplet sizes, leading to different impact outcomes and secondary phenomena, see Figure 1 for exemplary frames of the droplet wall-film interaction experiment monochrome camera images. The former analysis of the droplet splash dataset consisted of manually constructing the regime map of the parameter space of an ensemble of fluids by an expert [3].

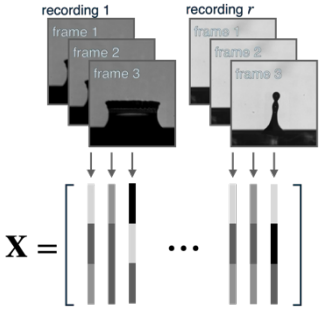

Figure 1. Stacking of recording frames to construct $\mathbf{X}$.

Goals and methods: The droplet splash recordings were performed in a more controlled, static setting compared to the mobile eye-tracking data. This study aims to introduce nonnegative matrix factorization to the analysis of droplet wall-film interaction. The NMF-based approach enables an exploratory analysis of multiple experiment recordings. Due to the natural interpretability of NMF, the usage is twofold: (1) for the identification of secondary phenomena, e.g., jet or bubble, and (2) to automatically differentiate impact velocities, fluids, and droplet sizes for multiple experiment recordings. This analysis of the crown shape and temporal evolution is of great interest [4]. Finally, we demonstrate the limitations and usefulness of our approach with different numbers of analyzed recordings and NMF-components $k \in \mathbb{N}$.

Methods and Dataset

For the visual analysis, NMF, introduced by Paatero and Tapper [5], is used to decompose the input data $\mathbf{X}$ into the interpretable factors $\mathbf{W}$ and $\mathbf{H}$ for $k \in \mathbb{N}$ (as denoted in the following).
For $k \in \mathbb{N}$ and $\mathbf{X} \geq 0$, $\min \|\mathbf{X} - \mathbf{WH}\|_{\text{fro}}$ with $\mathbf{W} \geq 0, \mathbf{H} \geq 0$, such that

$$\mathbf{X} = \begin{bmatrix} | & & | & & | & & | \\ x_1^{(1)} & \cdots & x_{m_1}^{(1)} & \cdots & x_1^{(r)} & \cdots & x_{m_r}^{(r)} \\ | & & | & & | & & | \end{bmatrix} \simeq \mathbf{WH}$$

$$= \begin{bmatrix} | & & | \\ w_1 & \cdots & w_k \\ | & & | \end{bmatrix} \cdot \begin{bmatrix} h_{1,1}^{(1)} & \cdots & h_{1,t_1}^{(1)} & \cdots & h_{1,1}^{(r)} & \cdots & h_{1,t_r}^{(r)} \\ \vdots & & \vdots & & \vdots & & \vdots \\ h_{k,1}^{(1)} & \cdots & h_{k,t_1}^{(1)} & \cdots & h_{k,1}^{(r)} & \cdots & h_{k,t_r}^{(r)} \end{bmatrix}.$$

spatial components — temporal components — representative images

This decomposition leads to pairs of spatiotemporal components (w_j, h_j) for each NMF component $j \in \{1, \ldots, k\}$. As a result, each spatial component w_j can be embedded back into the image domain and the associated temporal component h_j (consisting of queued temporal components for each recording) is split into multiple vertically

arranged line charts, denoted as temporal indicator plots. These plots directly indicate the most relevant frames for each recording, expressed and highlighted as the respective representative images from the recordings. All computations follow Berry et al. [6] and were performed in MATLAB.

The droplet splash dataset consists of a total of 1300 recordings of droplet wall-film interactions. It contains experiments with different droplet diameters (2.2 mm to 4.0 mm), droplet velocities (0.1 m/s to 5.0 m/s), and film thicknesses (0.1 mm to 1.3 mm). The liquids used for the droplet and wall-film include, among others, hexadecane (hexa), hyspin, water, diesel, and engine oil. For the vectorization, every 10-th frame is used to reduce the total runtime. The monochrome frames of each recording are stacked consecutively to be further processed with NMF, as illustrated in Figure 1.

Results and Discussion

The proposed NMF-based analysis was performed for different settings and configurations using the vast droplet splash dataset by Geppert [2]. For the scope of this work, we restrict the detailed analysis to the following two controlled sets of recordings: 50 hyspin-hexa droplet wall-film interactions and the broader analysis of 12 preprocessed recordings with different droplet-wall fluid combinations.

Analysis of hyspin–hexadecane interaction. For the initial analysis, 50 hyspin-hexa droplet wall-film interactions are decomposed into six spatiotemporal components (only the first 12 recordings are illustrated in Figure 2). The NMF decomposition enables the distinction between the background (component 6) and different temporal components, e.g., crown formation (component 2), crown detachment (component 4), and splashing (components 1 and 5). As a first step, this characterization can be directly stated through the different spatial representations that hint at specific phenomena, e.g., the crown detachment in component 4. Furthermore, taking the temporal indicator plots into account, the temporal occurrence of the phenomena can be taken into perspective, e.g., the splashing (component 5) that is present throughout the rest of recordings 3 to 12 but stops early in recordings 1 and 2. Finally, the representative images show the specific maxima for each indicator plot and confirm the characterization, see component 2. Specifically, components 1, 4, and 6 show misleading results for the thin wall film (either being red or white). Filtering the recordings by subtracting the first frame leads to more comprehensible results, as the second analysis shows.

Analysis of droplet wall-film interactions for different fluids. For the second analysis, the investigated experiments are broadened to reflect different behaviors after the droplet impact, e.g., secondary phenomena. The investigated droplet wall-film combinations include hyspin-hexa (0.27, 0.23, 0.24, 0.25), diesel-engine oil (0.26, 0.74), hyspin-hyspin (0.26, 0.26), and hexa-hexa (0.25, 0.22, 0.51, 0.51), where the numbers in brackets denote the measured film thickness (in mm). Furthermore, the background noise is filtered out via subtraction of the respective first frame for each recording. As displayed in Figure 3, NMF successfully decomposes the dataset into different impact outcomes and secondary phenomena, e.g., the lamella (component 2) and resulting jet (component 5), as well as crown detachment (components 1, 4, and 6). Compared to the previous analysis, the filtering leads to more precise spatial representations and representative images. Furthermore, the temporal indicator plots show the temporal occurrence of the secondary phenomena and, therefore, enable the differentiation between impact velocities, fluids, and droplet sizes. This is specifically visible for component 5, where the indicator plots only show high impacts for

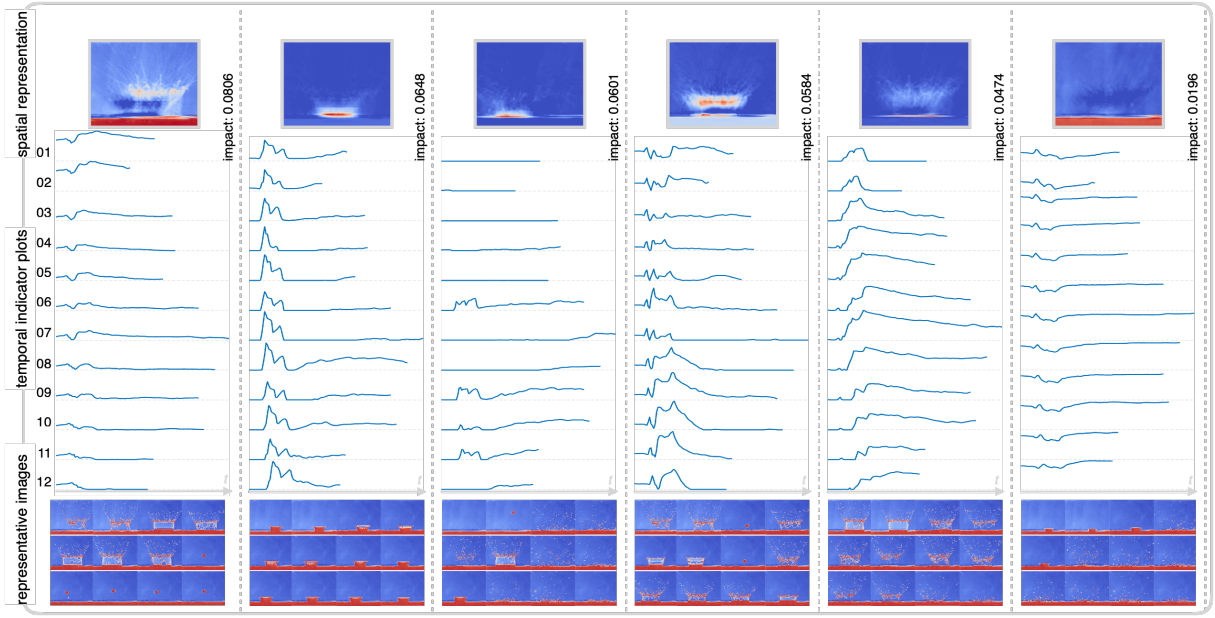

Figure 2. Application of our NMF-based visual analysis on 50 hyspin-hexa droplet wall-film interaction recordings. The data was decomposed into six spatiotemporal components and only the first 12 recordings are shown in the temporal indicator plots and representative images.

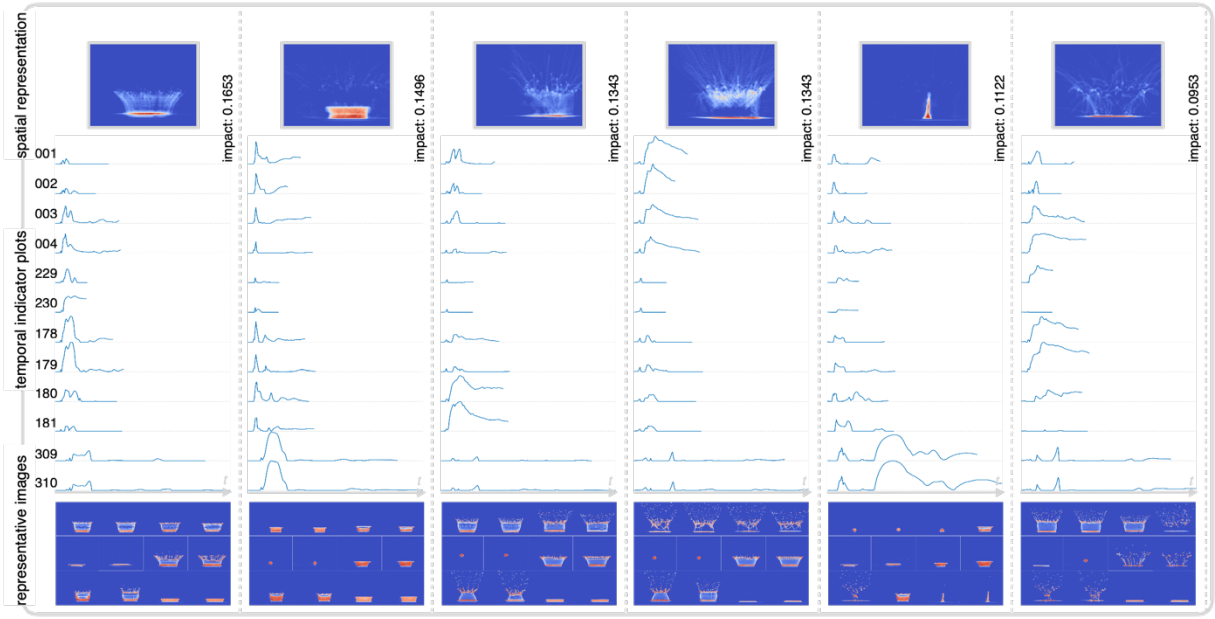

Figure 3. Application of our NMF-based visual analysis on 12 droplet wall-film interaction recordings with different droplet wall-film combinations, e.g., hyspin-hexa (0.27, 0.23, 0.24, 0.25), diesel-engine oil (0.26, 0.74), hyspin-hyspin (0.26, 0.26), and hexa-hexa (0.25, 0.22, 0.51, 0.51). The numbers in bracket denote the measured film thickness (in mm). The preprocessed data was decomposed into six spatiotemporal components.

recordings 309 and 310. Also, the lamella in component 2 is clearly visible and longer-lasting for these recordings. Again, the representative images confirm these observations. Very similar experiment configurations, e.g., recordings 180 and 181, as well as 229 and 230, also show similar temporal indicator plots in the NMF decomposition. In a similar analysis, we also included diesel-diesel droplet wall-film combinations. They are characterized via very long-lasting bubble formation as secondary phenomena. In the visual analysis, the resulting bubble wiped out all small-scale features in the spatial representations by arising for each of the components. Therefore, we excluded these experiments in the investigated set of configurations.

Discussion. To sum up, the extraction and distinction of different secondary phenomena is possible using the NMF-based analysis framework. This holds especially for the impact outcomes “jet” or “bubble.” The reduction of background noise, as well as a static viewpoint, is beneficial for the outcome of the analysis and should be included as a preprocessing step. To improve the decomposition even more, the recordings should be centered around the droplets for future studies. One goal of the study was to analyze multiple recordings simultaneously. While the study showed promising results for low recording numbers, the analysis with more than 200 recordings showed non-distinct results. Due to the broad information in the recordings, the spatial representations are mixed and specific impact outcomes and secondary phenomena are not isolated in the NMF components. Another limitation is the number of NMF components. If it is set too low, not enough features can be extracted, and for a high number of components ($k > 30$), specific frames were extracted, e.g., non-filtered background features or artifacts. One promising aspect for future work is the problem-specific (numerical) analysis of the temporal components ($-h_i -$). This could lead to better interpretability and comparability between specific recordings. Furthermore, similar components, identified via Wasserstein distance computation, could be clustered to reduce the number of spatiotemporal NMF components in post-processing.

Acknowledgments

This work was supported by the Deutsche Forschungsgemeinschaft (DFG, German Research Foundation) – Project-ID 270852890 – GRK 2160/2.

References

[1] D. Klötzl, T. Krake, F. Heyen, M. Becher, M. Koch, D. Weiskopf, and K. Kurzhals, “NMF-based analysis of mobile eye-tracking data,” in Proceedings of the Symposium on Eye Tracking Research and Applications, article no. 76, 2024.

[2] A. K. Geppert, “Experimental investigation of droplet wall-film interaction of binary systems,” Dissertation, University of Stuttgart, 2019.

[3] A. Geppert, A. Terzis, G. Lamanna, M. Marengo, and B. Weigand, “A benchmark study for the crown-type splashing dynamics of one- and two-component droplet wall-film interactions,” Experiments in Fluids 58, article no. 172, 2017.

[4] I. V. Roisman and C. Tropea, “Impact of a drop onto a wetted wall: description of crown formation and propagation,” Journal of Fluid Mechanics 472, 373–397, 2002.

[5] P. Paatero and U. Tapper. “Positive matrix factorization: A non-negative factor model with optimal utilization of error estimates of data values,” Environmetrics 5(2), 111–126, 1994.

[6] M. W. Berry, M. Browne, A.N. Langville, V. P. Pauca, and R. J. Plemmons, “Algorithms and applications for approximate nonnegative matrix factorization,” Computational Statistics and Data Analysis 52(1), 155–173, 2007.

Investigation of Droplet-Pool Phenomena and Droplet-Film Interaction for Immiscible Fluids

R. Dhar, K. Schulte
Institute of Aerospace Thermodynamics (ITLR), University of Stuttgart
*Corresponding author: rishi.dhar@itlr.uni-stuttgart.de

Introduction

Over a century of research on droplet interactions with deep pools [1] and films [2] have facilitated numerous industrial and research applications [3], such as inkjet printing [4], and spray cooling of electronic components [5]. From a practical standpoint, applications such as engine fuel injection involve the interaction of fuel droplets with thin films of engine oil, which are immiscible [6]. While extensive work has been done on droplet-film interactions with same liquids [7,8,9], the literature suggests that there are still many complexities within immiscible fluid interactions that remain incompletely understood. For instance, Che and Matar [10] conducted an experimental study on a droplet impinging an immiscible film liquid by varying the fluid properties for the drop and the film as well as varying the film thickness. In one case, when a water droplet impacted a silicon B15 oil film, a compound crown with separate rims of the drop and the film liquid formed. Conversely, when a silicon B15 oil drop impacted a water film, the oil adhered to the edge of the water film layer till the rim level. However, a comprehensive understanding and modelling of the influence of the fluid properties and their ratio on the impact outcome is still missing. Furthermore, Kittel [11] observed that the film thickness affected the dynamics of immiscible drop-film interactions significantly. Our aim is gaining a deep understanding of the underlying physical mechanisms using Direct numerical simulations. Free Surface 3D (FS3D), a multiphase flow package developed at ITLR [12], has demonstrated potential in investigating drop-film interactions [13], also for miscible fluids [14]. As a next step, the following study is presented to assess the feasibility of FS3D for the direct numerical simulation of drop impact on immiscible films.

In order to classify the droplet-liquid interaction scenarios, a non-dimensional number (δ) which is the ratio of the film height (h) and diameter of the droplet (D_0), segregates cases in four categories; droplet pool interactions (δ > 4), droplet thick film or shallow pool interaction (4 > δ > 0.6), droplet thin film interaction (0.6 > δ > 0.08) and droplet-very thin film interaction (0.08 > δ) [15]. Considering the multi-scale nature of the immiscible droplet-film interactions, a simplified setup of droplet-pool scenario had been considered (δ > 4) for validation where the solid surface properties had no influence on the impact outcome. A good qualitative agreement with the data of the experimental study by Castillo-Orozco [16] on a silicon B5 oil drop impacting a pool could be shown.

Numerical Setup and Results

FS3D, used for the current work, performs direct numerical simulations (DNS) while solving the incompressible Navier-Stokes equations with the volume-of-fluid (VOF) method. In order to avoid numerical diffusion, the interfaces are reconstructed using a piecewise linear interface computation (PLIC) [17], which had been adapted for the simulation of three phase problems [18]. Surface tension forces in FS3D can be computed using different approaches, including an adapted Continuum Surface Stress (CSS) method [18], which had been used in the current study.

The setup is depicted in Fig. 1. A grid size of 9.7 D_0 x 9.7 D_0 x 9.7 D_0 and the pool height of 4 D_0 was found to be sufficient to capture the crater and jet formation observed in experimental data [16]. A symmetry in the x=0 and y=0 direction had been used to reduce the computational cost and enable a high resolution of the droplet. A silicon B5 oil droplet of diameter (D_0) 1.8 mm released from top, impacted the pool of same liquid with a Weber (We) number of 230.

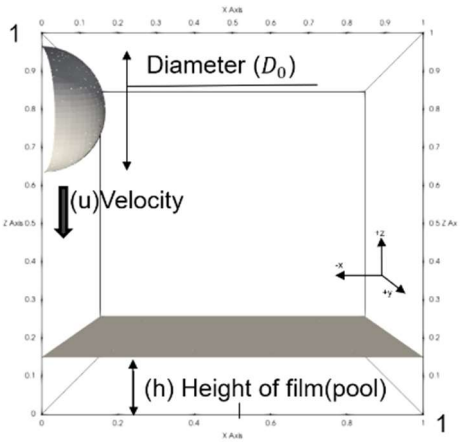

Figure 1. A setup for drop-film (pool) simulation

A grid refinement study on droplet-film interactions with miscible fluids, conducted by Steigerwald [14], demonstrated that a resolution of approximately 140 cells per droplet diameter is sufficient to accurately capture the crown and rim structures. Also in the current study, a resolution of 110 cells per diameter (1024^3 cells) showed a good agreement with the experimentally observed crater depth of 2.5 D_0 at 10 ms after impact, where t = 0 corresponded to the moment of droplet impact.

Apart from the good convergence with the crater depth during grid independence study, FS3D could also capture the Rayleigh jet height accurately just before the detachment of the secondary droplet, which was observed experimentally to be approximately 5.6 D_0. Figure 2 depicts the qualitative good agreements of the simulation results and the experimental data at different time steps and proves the applicability of FS3D for the immiscible drop impact.

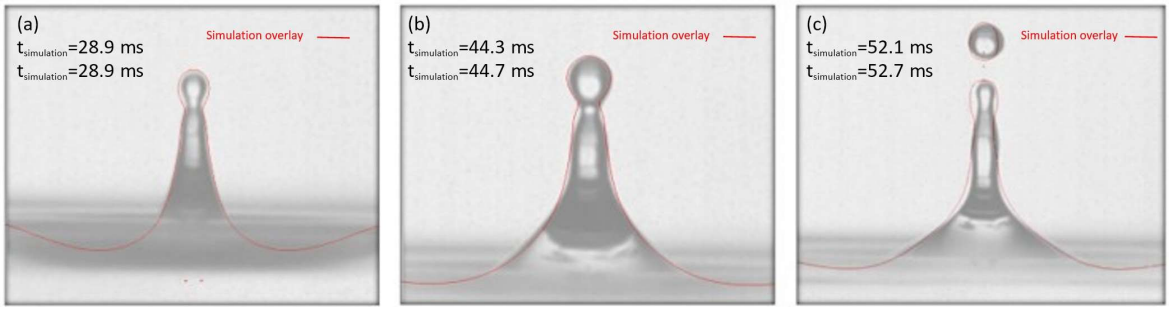

Figure 2. Comparison of experimental results of Castillo-Orozco [16] with simulation results at different time steps for drop-pool scenarios: (a) Secondary jet formation (b) Jet formation before detachment (c) Secondary droplet detachment from jet.

Conclusion and Outlook

The good agreement between the numerical and experimental data in the current study demonstrated that FS3D effectively captures the dynamics of droplet-pool interactions of immiscible liquids.

Comprehensive numerical studies will provide a fundamental understanding of the underlying mechanisms responsible for the observed phenomena, with particular focus on varying the viscosity ratio between the droplet and film liquids. Additionally, film thickness will be adjusted to assess its influence on splash dynamics.

References

[1] Arthur Mason Worthington. *A study of splashes*. Longmans, Green, and Company, 1908.

[2] William D Harkins and Aaron Feldman. The spreading of liquids and the spreading coefficient. *Journal of the American Chemical Society*, 44(12):2665-2685, 1922.

[3] P. V. Hobbs and T. Osheroff. Splashing of drops on shallow liquids. *Science 158*, 3805:1184-1186, 1967.

[4] Dirkjan B. van Dam and Christophe Le Clerc. Experimental study of the impact of an ink-jet printed droplet on a solid substrate. *Physics of Fluids 16*, 9:3403-3414, 2004.

[5] Jungho Kim. Spray cooling heat transfer: The state of the art. *International Journal of Heat and Fluid Flow 28*, 4:753-, 2007.

[6] Malki Maliha et al. Optical investigation on the interaction between a fuel-spray and an oil wetted wall with the focus on secondary droplets. *International Journal of Engine Re-*

search 24, 4:1578–1588.

[7] Samah K. Alghoul, Carol N. Eastwick, and David B. Hann. Normal droplet impact on horizontal moving films: an investigation of impact behaviour and regimes. *Experiments in Fluids 50*, 5:1305–1316, 2010.

[8] Kuo-Long Pan et al. Collision dynamics of high-speed droplets upon layers of variable thickness. *Experiments in Fluids 45*, 3:435–446, 2008.

[9] Ilia V. Roisman, Kristijan Horvat, and Cam Tropea. Spray impact: Rim transverse instability initiating fingering and splash, and description of a secondary spray. *Physics of Fluids 18*, 10, 2006.

[10] Che Z. and Matar O. *Impact of droplets on immiscible liquid films*. Soft Matter, Issue 9, 2018.

[11] Hannah M. Kittel, Ilia V. Roisman, and Cameron Tropea. Splash of a drop impacting onto a solid substrate wetted by a thin film of another liquid. *Phys. Rev. Fluids*, 3:073601, July 2018.

[12] Kathrin Eisenschmidt et al. Direct numerical simulations for multiphase flows: An overview of the multiphase code FS3d. *Applied Mathematics and Computation 272 (Jan. 2016), pp. 508–517. issn:*, 0096-3003.:508-517, 2016.

[13] Stefan Schubert, Jonas Steigerwald, Anne K. Geppert, Bernhard Weigand, and Grazia Lamanna. Micro-piv study on the influence of viscosity on the dynamics of droplet impact onto a thin film. *Experiments in Fluids*, 65(5), April 2024.

[14] Jonas Steigerwald et al. Towards the numerical determination of the splashing threshold of two-component drop film interactions. *High Performance Computing in Science and Engineering '20. Springer International Publishing, 2021, pp. 261–279. isbn:*, page 9783030806026., 2021.

[15] A. Geppert, A. Terzis, G. Lamanna, et al. A benchmark study for the crown-type splashing dynamics of one- and two-component droplet wall-film interactions. *Exp Fluids 58*, 172, 2017.

[16] Eduardo Castillo-Orozco et al. Droplet impact on deep liquid pools:rayleigh jet to formation of secondary droplets. *Phys. Rev. E*, 92:053022, 2015.

[17] David Youngs. *Time-Dependent Multi-material Flow with Large Fluid Distortion*, volume 24, pages 273–285. 01 1982.

[18] Johanna Potyka and Kathrin Schulte. A volume of fluid method for three dimensional direct numerical simulations of immiscible droplet collisions. *International Journal of Multiphase Flow*, 170:104654, January 2024.

New approaches to modelling heat/mass transfer processes in spherical and non-spherical mono-component droplets

S.S. Sazhin[*1,2,3,4], S. Tonini[4], G.E. Cossali[4], D.V. Antonov[3], P.A. Strizhak[3]

[1]Advanced Engineering Centre, School of Architecture, Technology and Engineering, University of Brighton, Brighton, BN2 4GJ, United Kingdom

[2]Kutateladze Institute of Thermophysics, Siberian Branch of the Russian Academy of Sciences, 1 Lavrentiev Avenue, Novosibirsk 630090, Russian Federation

[3]National Research Tomsk Polytechnic University, 30, Lenin Avenue, Tomsk, 634050, Russian Federation

[4]Department of Engineering and Applied Sciences, Università degli Studi di Bergamo, Viale Marconi 6, 24044 Dalmine (BG), Italy

*Corresponding author: S.Sazhin@brighton.ac.uk

Introduction

The importance of accurately modelling the heating and evaporation of spherical and non-spherical droplets is well known and has been described in numerous papers and books summarised in the monographs [4, 5]. These processes have many industrial applications, including spray drying and combustion, some of which are discussed in [4, 5]. This abstract is focused on a brief analysis of new approaches to modelling heat/mass transfer processes in spherical and non-spherical mono-component droplets, obtained after the publication of [4, 5].

Material and methods

The abstract is focused on the analysis of spherical and spheroidal droplets heated in ambient gas (air), based on a combination of analytical and numerical methods. The analytical solutions of heat and mass transfer equations in the gas and liquid phases were obtained, if possible. Then these solutions in the gas phase were used as boundary conditions for the liquid phase. Thus the new analytical-numerical method was developed and applied to a specific problem of droplet heating and evaporation. In this method the predictions of the analystical or numerical solutions at the end of each time step are used as initial conditions for the following time steps with updated values of input parameters

Results and Discussion

Recent developments in the modelling of heating and evaporation of spherical and non-spherical mono-component droplets ([6, 2, 1, 3]) are reviewed. These include the model linking the previously developed liquid phase model, using the analytical solution to the heat transfer equation at each time step, and the gas phase model, using the solution to the equations of the conservation of mass, momentum, and energy leading to an explicit expression for the Nusselt number and implicit expression for evaporation rate of the droplet [2] (called Model 3). The predictions of the numerical algorithms for this and the previously developed approaches are compared with experimentally observed time dependencies of the rates of change of radii and average temperatures of n-decane droplets at initial temperatures and radii equal to 300 K and 0.85 mm, respectively, placed in a gas at temperature 760 K. The results of the comparison are shown in Figure 1. In Model 1, to which Figure 1 refers, the heat rate, supplied to the droplets to raise their internal energy, is calculated based on the observation that steady-state equations for heat and mass balance in the gas phase should lead to the same droplet evaporation rates. The direct calculation of the above-mentioned heat rate is used in Model 2; the value of this rate is then used for the estimation of the droplet evaporation rate using the Spalding heat transfer number [1].

It can be seen from Figure 1 that the experimentally observed $\dot{R}_d$ and $\dot{T}_d$ are reasonably close to those predicted by Model 3. The deviations between the observed values of $\dot{R}_d$ and $\dot{T}_d$

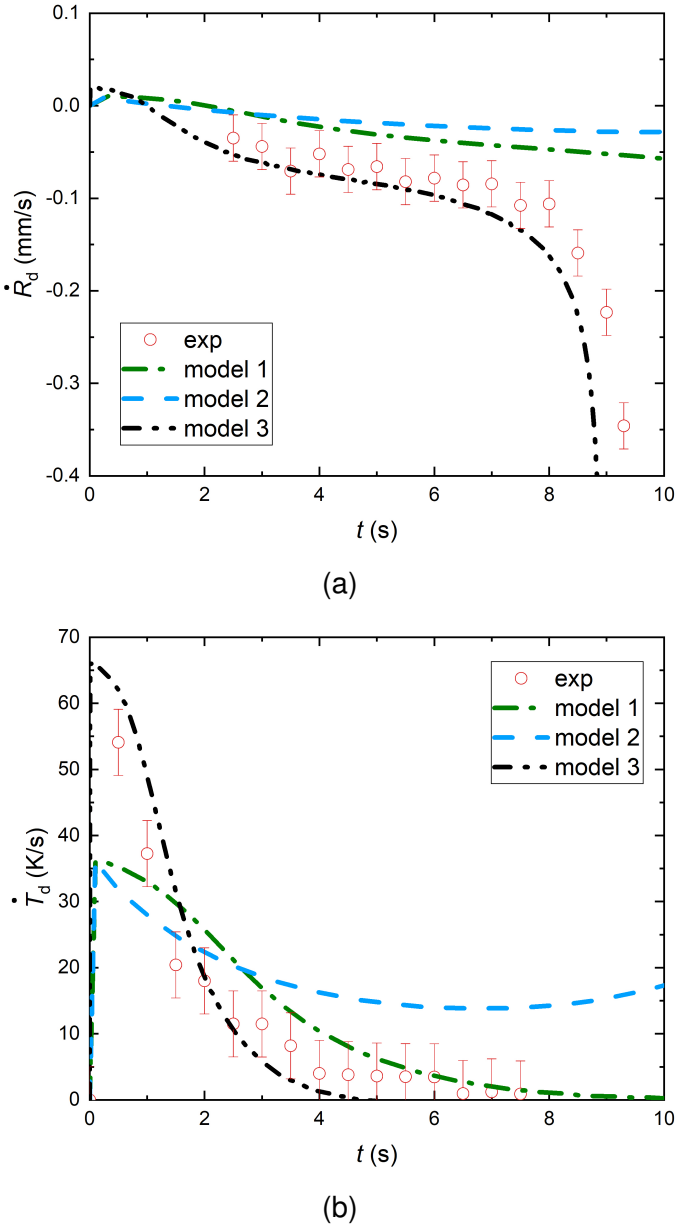

Figure 1. Plots of rate of change of radius ($\dot{R}_d$) and average temperature ($\dot{T}_d$) of an n-decane droplet versus time predicted by Models 1, 2 and 3 and observed experimentally (exp). Gas temperature T_g was 760 ± 10 K; initial droplet temperature (T_{d0}) and radius (R_{d0}) were 300 ± 10 K and 0.85 ± 0.05 mm, respectively. Copyright Elsevier (2024)

and those predicted by Models 1 and 2 are are quite large. These models even predict different trends of change for these parameters, which limits their suitability for studying the time evolution of these parameters during droplet heating/evaporation. The trends similar to those illustrated in Figure 1 were also shown for for the ambient gas temperature equal to 500 ± 10 K. A mathematical model for spheroidal droplet heating and evaporation takes into account the effect of liquid finite thermal conductivity and is based on the previously obtained analytical solution for the vapour mass fraction at the droplet surface and a new correlation for the convective heat transfer coefficient incorporated into the numerical code. The heat transfer equation in the liquid phase is solved numerically using the finite element heat transfer module of COMSOL Multiphysics [3].

It is shown that the lifetimes of prolate and oblate droplets is shorter than that of spherical droplets of the same volume. The difference in these lifetimes is shown to increase with increasing aspect ratios for prolate droplets and decreasing aspect ratios for oblate droplets. The predictions of the model are shown to agree with experimental data. The maximal surface tem-

peratures are predicted near the areas with the maximal surface curvatures. The aspect ratios were shown to be weakly dependent on time, which is consistent with experimental data.

Conclusion

A recently developed model of heating and evaporation of spherical droplets is described. This model links the previously developed liquid phase model, using the analytical solution to the heat transfer equation at each time step, and the gas phase model, based on the solution to the equations of the conservation of mass, momentum, and energy which leads to an explicit formula for the Nusselt number and a realtively simple equation for the evaporation rate of the droplet. It is shown that this model predicts the results closer to experimental data than the previously developed models.

A recently developed model for spheroidal droplet heating and evaporation is described. This model considered the effect of liquid finite thermal conductivity and is based on the analytical solution for the vapour mass fraction at the droplet surface and a correlation for the convective heat transfer coefficient. Both were incorporated into the numerical code.

Nomenclature

R	droplet radius [m]
t	time [s]
T	temperature [T]

Subscripts

d	droplet
g	ambient gas
0	initial

Acknowledgments

Financial support received from the Tomsk Polytechnic University development program, Priority 2030 (Priority-EB-018-202-2024), Ministry of Science and Higher Education of the Russian Federation (Grant 075-15-2024-620) (DA and SS) and the University of Bergamo (SS's visiting professorship) is gratefully acknowledged. The research presented in the paper was initiated during work on a project supported by the Royal Society (UK) (Grant no. IEC 192007).

References

[1] D. V. Antonov, S. Tonini, G. E. Cossali, M. Al Qubeissi, P. A. Strizhak, and S. S. Sazhin. *International Journal of Multiphase Flow*, 179:104922, 2024.

[2] D. V. Antonov, S. Tonini, G. E. Cossali, V. V. Dolgikh, P. A. Strizhak, and S. S. Sazhin. *Physics of Fluids*, 35:073311, 2023.

[3] D. V. Antonov, S. Tonini, G. E. Cossali, P. A. Strizhak, and S. S. Sazhin. *Applied Mathematical Modelling*, 125:687–703, 2024.

[4] G. E. Cossali and S. Tonini. *Drop Heating and Evaporation: Analytical Solutions in Curvilinear Coordinate Systems*. Springer, 2021.

[5] S. S. Sazhin. *Droplets and Sprays: Simple Models of Complex Processes*. Springer, 2022.

[6] S. Tonini, G. E. Cossali, E. A. Shchepakina, V. A. Sobolev, and S. S. Sazhin. *Physics of Fluids*, 34:073312, 2022.

The Influence of Heat Transfer on the Outcome of Droplet Collisions of Supercooled Water Droplets

V. Kunberger*[1], B. Weigand[1]
Institute of Aerospace Thermodynamics, University of Stuttgart, Germany
*Corresponding author: verena.kunberger@itlr.uni-stuttgart.de

Introduction

The phase change and interaction behavior of supercooled water droplets are crucial for understanding cloud formation and precipitation processes. These micro-processes are of relevance for the development and enhancement of climate models and weather forecasts [1].
In clouds, extreme ambient conditions with temperatures as low as -40° C lead to the supercooling of water droplets. During the freezing of the droplets, latent heat is released which is one of main energy sources in clouds or more severe weather phenomena like cyclones [2]. This also affects clouds on a macroscopic scale as droplets in the vicinity of the latent heat release evaporate and therefore the cloud size is limited [1].
Phase change is initiated by either homogeneous nucleation or by heterogeneous nucleation through particles like aerosols or ice crystals.

Due to convection, the supercooled water droplets are in constant motion in the clouds and interact and collide with each other. The result of these collisions is dependent on the nucleation, if it is triggered by the impact and also on the ambient conditions as the surrounding gas has to transport the latent heat released during the freezing process away. This is dependent on the conduction and convection properties of the ambience. Therefore, the rate of freezing is dependent on the surrounding gas and its heat transfer ability.

The freezing process of a droplet was described by Hindmarsh [3] and is shown in Figure 1.

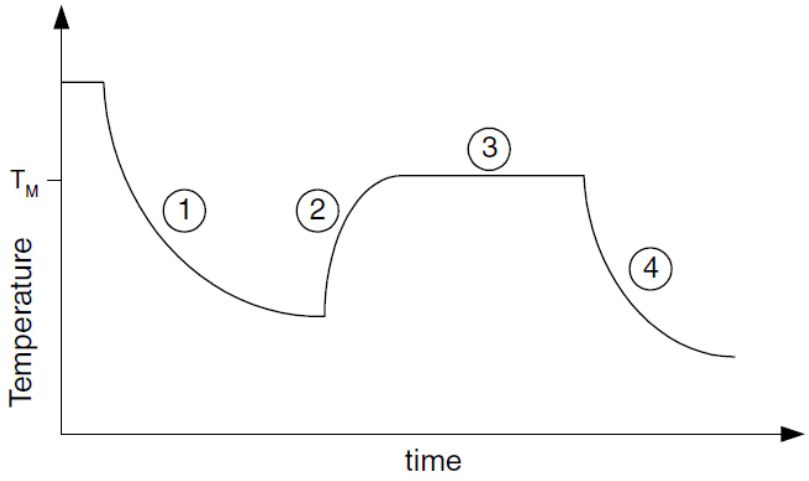

Figure 1. Freezing process of a droplet [3]

First, the droplet cools down to subzero temperatures and is supercooled. Then, nucleation starts and the temperature jumps to 0°C, the melting or freezing temperature, due to the release of latent heat. This heat has to be transported away and the frozen droplet then cools down to ambient temperature.

For droplet collisions of supercooled water droplets, it is important to know how fast this transport of the latent heat is to interpret the experimental results.

Analytical Model

Around the supercooled droplet several heat and mass transfer processes take place that are depicted in Figure 2. The droplet freezes from outside to inside, so there is an outer ice shell while on the inside is mushy ice that is not completely frozen due to the latent heat release from nucleation. Through the ice shell, heat is conducted to the outside. There, convection due to the nitrogen flow transports the heat away. Furthermore, there is sublimation/evaporation and diffusion happening at the droplet surface.

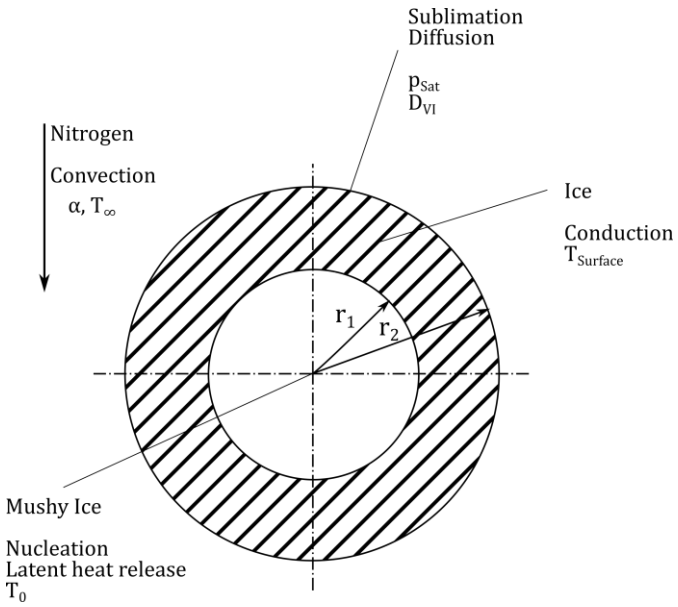

Figure 2. Heat and mass transfer processes around a droplet

For our modeling of the heat transfer processes some assumptions were made. First, the latent heat is released all at once and the temperature distribution within the droplet is uniform. Furthermore, the conduction is neglected. Fluid properties were taken from the NIST REFPROP database.
The following Nusselt correlation was used for the convection process

$$Nu = 2 + (0.4Re^{\frac{1}{2}} + 0.06Re^{\frac{2}{3}})Pr^{0.4}\left(\frac{\eta_\infty}{\eta_S}\right)^{1/4} \quad (1)$$

which leads to the heat transfer coefficient *h* and therefore the convection heat flux [4].

$$\dot{Q}_{konv} = hA(T_S - T_\infty) \quad (2)$$

This heat flux will transport the latent heat away in a certain time and we can equate the two.

$$Q_{LH} = \dot{Q}_{konv}\, t \quad (3)$$

By that, we can gain the time that is needed for complete freezing until all of the latent heat is transported away.

Results and Discussion

For varying Reynolds numbers for a droplet size of 45 µm and a relative humidity of 0.5, the results are shown in Figure 3.

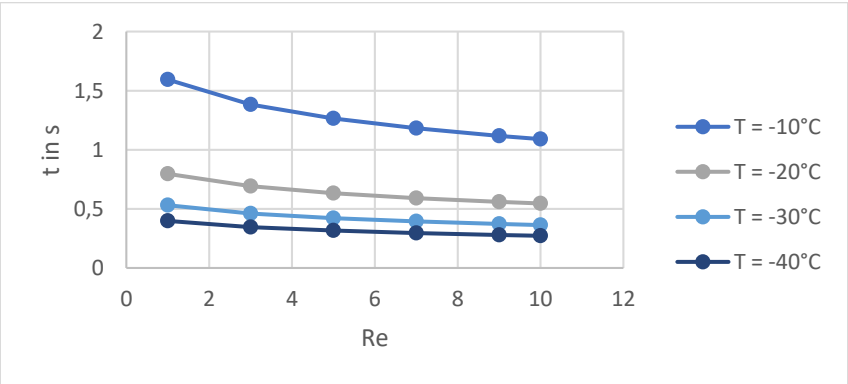

Figure 3. Freezing times for a 45 µm droplet at relative humidity of 0.5

It can be seen that even for low supercooling of -10°C, the freezing process is relatively fast with 1.5 seconds and the time decreases for higher supercooling.
Also the droplet size was varied at a constant Reynolds number of Re = 5 and relative humidity of 0.5, the results are shown in Figure 4.

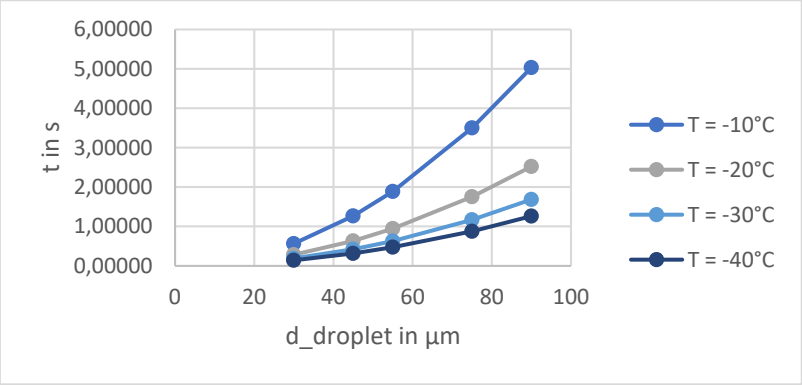

Figure 4. Freezing times for a droplet at Re = 5 and relative humidity of 0.5

For larger droplet sizes above 100 µm, the freezing time increases to more than 5 seconds for a supercooling of -10°C. For high supercooling of -40°C, the freezing time remains short, around 1 second.

For our droplet collision experiments this means, that all collisions happen when the levitated droplet is completely frozen as we cannot release a second droplet within a second. But we also see that for larger droplets, the timescale of freezing is of relevance and can influence the collision results.

The evaporation at the surface was also modeled but the results with and without evaporation did not change significantly.

Nomenclature

Nu	Nusselt number
Re	Reynolds number
Pr	Prandtl number
T	Temperature [°C]
η	dyn. Viscosity [Pa s]
h	Heat transfer coefficient [W/m²K]
$\dot{Q}$	Heat flux [W]
Q	Heat [J]

References

[1] Pruppacher, H. R., Klett, J. D., 1997, 'Microphysics of clouds and precipitation'. Kluwer Academic Publishers.
[2] A. Khain, M. Ovtchinnikov, M. Pinsky, A. Pokrovsky, H. Krugliak, 2000, Atmospheric Research, 55(3), pp. 159-224.
[3] J.P. Hindmarsh, A.B. Russell, X.D. Chen, *Experimental and numerical analysis of the temperature transition of a suspended freezing water droplet,* International Journal of Heat and Mass Transfer 46 (2003) 1199–1213
[4] Whitaker, S. (1972), Forced convection heat transfer correlations for flow in pipes, past flat plates, single cylinders, single spheres, and for flow in packed beds and tube bundles. AIChE J., 18: 361-371

Splashing Modes in Droplet Impacts onto Sub-Millimeter Microstructures

P. Palmetshofer*[1], A. Geppert[1], B. Weigand[1]
Institute of Aerospace Thermodynamics, University of Stuttgart, Germany
*Corresponding author: patrick.palmetshofer@itlr.uni-stuttgart.de

Introduction

Predicting whether splashing occurs in a droplet impact is important in a variety of technical applications, such as spray painting, plant-protective agent application and in fluid injection into combustion chambers [1]. In many cases, impacting droplets can interact with structure sizes which are smaller, but of similar magnitude as the droplet diameters. While no universal splashing limit has been found for rough or structured surfaces with small feature sizes, empirical correlations for splashing have been reported in the literature [2,3]. However, the effect of larger surface structures on the splashing limits has not been explored as thoroughly. Thus, in the scope of this study, we investigate whether existing splashing limits can predict the onset of splashing on structures which are only one order of magnitude smaller than an impacting droplet and explore the different splashing modes which can occur on such surfaces. In the following, after giving the experimental methods, splashing is split into prompt, finger and ligament splashing and possible limitations for all phenomena are discussed.

Experimental Methods

To record the droplet impact process, we use our four-perspective imaging setup, which uses three high-speed cameras. The top and lateral views are combined onto a single sensor as shown in figure 1, using a Photron SA-X2 high speed camera at 20 000 fps. The same camera model is used in synchronized mode for the bottom view, which is configured as a total internal reflection view to accurately track the contact lines. Lastly, a Krontech Chronos 1.4 is used for the spatial view, which is an inclined lateral view at a 90° offset with respect to the other lateral view. This camera records the impact process at a frame rate of 2500 fps. The impact parameters (droplet diameter and velocity) are determined automatically using a MATLAB script, which processes the images of the lateral view.

Three types of surface samples are used, all featuring cubic pillars on a square grid with side lengths, heights and separations of 0.1 mm, 0.2 mm and 0.5 mm. The surfaces were manufactured by LightFab GmbH Germany through selective laser etching of fused silica glass. The inherent wettabilities of the surfaces are changed between superhydrophilicity and hydrophobicity through plasma polymerization and plasma activation. The water and isopropanol droplets are dropped from a falling height of 0.15 m, 0.3 m, 0.7 m, and 1.2 m, through regular detachment from a needle with a diameter of 0.4 mm.

Results and Discussion

For droplet impacts onto sub-millimeter structures, we observe two distinct splashing regimes: prompt splashing and finger splashing. In prompt splashing, small secondary droplets are ejected at low angles. Finger splashing involves the ejection of larger fingers almost vertically, which only later break apart into secondary droplets. While no clear mechanism has been established for finger splashing, fluid redirection within grooves appears to play a role, and even at lower impact velocities, the fluid can be redirected upward, forming vertical liquid fingers that later disintegrate due to the Plateau-Rayleigh instability.

Although these two splashing modes are distinct, differentiating between them can be difficult, especially because both phenomena can occur within a single impact process.

When examining the different splashing modes, certain patterns emerge: In smaller structures, prompt splashing tends to dominate, and the liquid forms a lamella that spreads across the tops of the pillars, which inhibits finger growth. For larger structures, finger splashing becomes more pronounced, as the upward redirection of liquid is less likely to be suppressed by the lamella. The thickness of the redirected liquid sheet appears to play a critical role in determining whether finger splashing will occur. This thickness depends on several factors, including the impact velocity, surface tension, and the size of the gap between the structures. Smaller structures encourage lamella formation, while larger structures promote finger splashing, which points to a clear structure-size dependency in the splashing behavior.

For prompt splashing, we investigate an existing splashing limit proposed by Foltyn et al. [3]: As shown in figure 1, the correlation appears to work well for hydrophilic surfaces with structure sizes of 0.1 mm and 0.2 mm. However, for the 0.5 mm structures, Foltyn's correlation tends to overpredict the splashing limit, suggesting that additional factors influence the splashing threshold. The correlation also struggles with hydrophobic surfaces, where the splashing limit is lowered further.

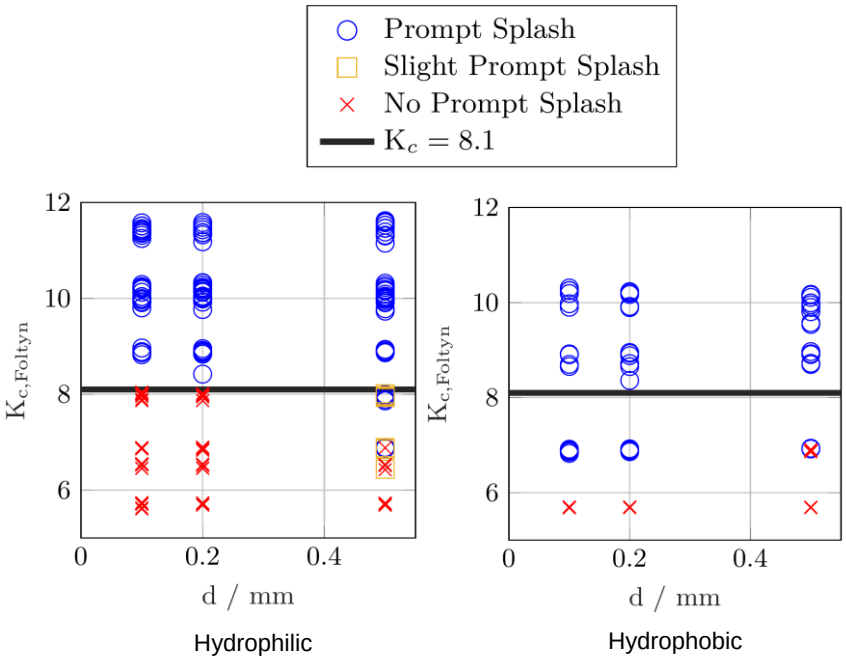

Figure 1: Prompt splashing limits for hydrophilic surfaces and hydrophobic cases.

For finger splashing, a splashing limit has been identified based on the structure-specific Weber number,

$$We_d = \frac{\rho U_0^2 d}{\sigma}$$

where ρ is the liquid density, U_0 is the impact velocity, d is the characteristic size of the structures and σ is the surface tension. The structure-specific Weber number is thus a parameter that accounts for the size of the surface features. This value seems to define a relatively clear threshold for finger splashing as shown in figure 2. However, it is suspected that additional factors, such as the Reynolds number and the ratio of structure size divided by droplet diameter, may further influence the splashing behavior. To better understand these dependencies, further measurements across a broader range of impact conditions, surface types, and droplet sizes are required. Numerical simulations could also help confirm this Weber number threshold and reveal more about the complex mechanisms driving finger splashing.

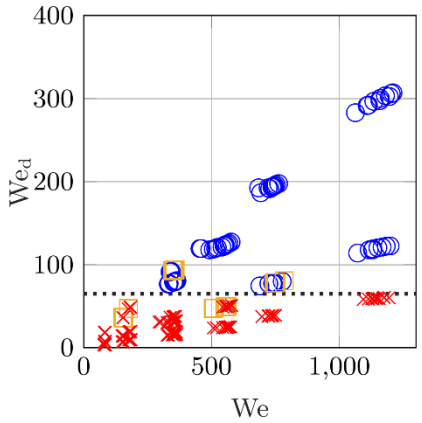

Figure 2: Finger splashing limits for all wettabilities

In addition to the primary splashing modes discussed, hydrophobic surfaces exhibit an additional splashing mode shown in figure 3, characterized by the ejection of droplets at shallow angles within the grooves. This behavior is here referred to as ligament splashing, where liquid jets propagate along the grooves of the surface structures and break up, as opposed to spreading more evenly across the surface. These jets tend to detach from the sides of the pillars and groove bottoms, eventually forming ligaments that break up due to the Plateau-Rayleigh instability. Observing and analyzing this splashing mode in greater detail requires further high-speed imaging and

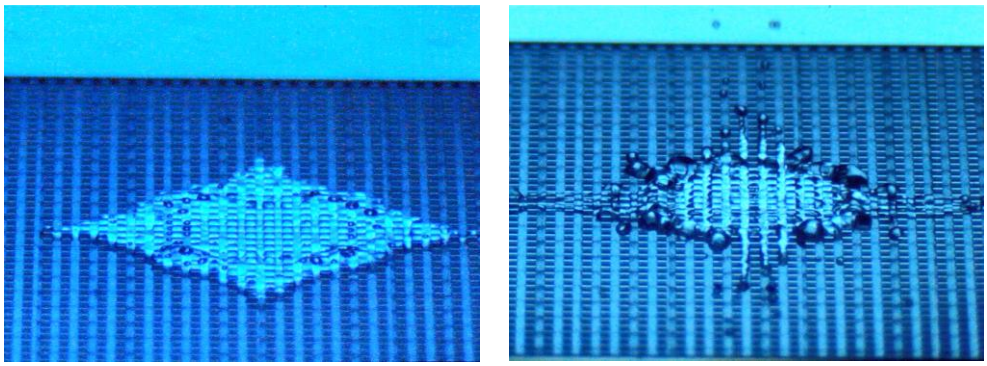

Hydrophilic Hydrophobic

Figure 3: Illustration of spreading on hydrophilic surfaces versus ligament splashing on hydrophobic surfaces

further studies to identify the ejection angles and conditions that contribute to this unique phenomenon. Overall, a deeper investigation into surface wettability and structure size is needed to fully define the splashing limits for both hydrophilic and hydrophobic surfaces, particularly in the context of groove jetting and other splashing mechanisms.

Conclusion

While existing splashing limits can predict prompt splashing well for hydrophilic 0.1 mm and 0.2 mm structures, corrections for hydrophobic surfaces [4] and larger structures are necessary. Additionally, to adequately predict the overall splashing limit, a distinction into prompt splashing, finger splashing and ligament splashing is necessary. While a structure-specific Weber number appears to be predictive for finger splashing, more investigations are necessary to provide a physically sound limit for finger splashing.

References

[1] Peduto, D.: *Oil Droplet Impact Dynamics in Aero-Engine Bearing Chambers - Correlations derived from Direct Numerical Simulations*. en, 2015. doi: 10.5445/IR/1000047740.

[2] Tsai, R. C. A. van der Veen, M. van de Raa, and D. Lohse, *How micropatterns and air pressure affect splashing on surfaces*, Langmuir 26, 16090–16095 (2010).

[3] Foltyn, P., Ribeiro, D., Silva, A., Lamanna, G., and Weigand, B.*: Influence of wetting behavior on the morphology of droplet impacts onto dry patterned micro-structured surfaces*. Physics of Fluids, 2022, 34 (12), p. 123322. doi: 10.1063/5.0124692.

[4] Zhang, H., Zhang, X., Yi, X., He, F., Niu, F., and Hao, P.*: Effect of wettability on droplet impact: Spreading and splashing*. Experimental Thermal and Fluid Science, 2021, 124, p. 110369. issn: 0894-1777. doi: 10.1016/j.expthermflusci.2021.110369.

Investigation of the Asymmetry of the Flow Field at the Wall during an Oblique Droplet Impact onto a Thin Wall Film

J.L. Stober, K. Schulte
Institute of Aerospace Thermodynamics (ITLR), University of Stuttgart
*Corresponding author: jonathan.stober@itlr.uni-stuttgart.de

Introduction

In most spray impact scenarios in technical applications, many droplets impact obliquely on a wetted wall. The mechanisms behind the formation of the asymmetric crown and splashing during the oblique droplet impact are not yet fully understood.

Yarin and Weiss [1] described the flow during a normal droplet impact by an inner wall film that spreads radially as a stagnation point flow, and an outer undisturbed wall film, as well as a kinematic discontinuity, that forms between it and where the crown sheet is ejected upwards. Roisman and Tropea [2] applied this analytical description on oblique impacts by assuming it as a normal impact onto a flowing wall film, hence a symmetric stagnation point flow as an inner wall film and a constantly flowing outer wall film. Under this assumption, they described the asymmetry of crown formation analytically.

However, the inner wall film flow during the oblique impact is still insufficiently characterized. In this contribution, the asymmetry of the flow field of the inner wall film, which generates the uprising crown, is investigated by means of direct numerical simulation, to understand the asymmetry on crown formation during the oblique droplet impact.

Numerical Setup

We apply the direct numerical program package Free Surface 3D (FS3D), that solves the incompressible Navier-Stokes equations for multi-phase flows using a volume-of-fluid method (VOF), [3]. The use of a symmetry plane ($y = 0$) reduces computational costs, see Fig 1A. The domain consists of a structured Cartesian grid which is equidistant in x- and y-direction with 1536 and 768 cells, respectively. In z-direction, 768 cells are used and the grid is refined close to the wall for a better resolution of the wall film flow. For $z \in [0, 0.1D_0]$ the resolution was doubled, which is shown in Figure 1B by visualizing every fourth grid line.

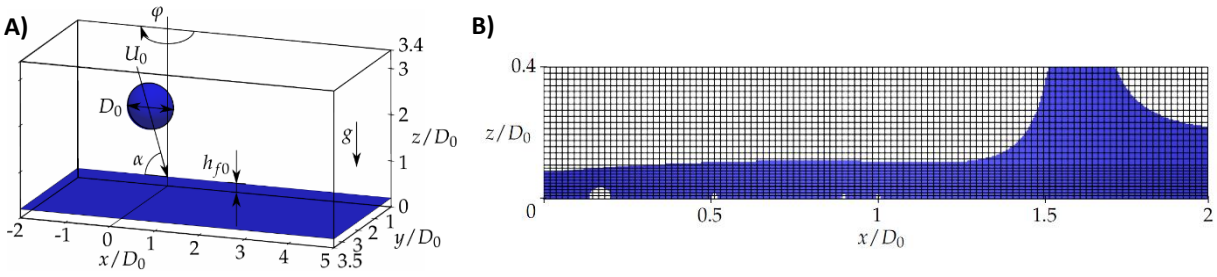

Figure 1. A) Sketch of the computational domain, B) visualization of the grid refinement at the wall, every fourth grid line is shown.

The impacting droplet is initialized with its diameter D_0, velocity U_0 and an impact angle α at a vertical distance of $1D_0$ above the wall film measured from its lower end. The droplet impacts the wall film at $x = 0 = y$. The wall film is initialized with a height of h_{f0} and consists of the same liquid. A symmetry boundary condition is set at $y = 0$, and a free-slip wall at the bottom $z = 0$. All other boundaries use zero gradient condition.

In this study an oblique impact with $\alpha = 70°$ of an isopropanol (ρ, μ, σ) droplet ($D_0 = 1.5$ mm) onto a liquid film of the same fluid is investigated, with air as ambient gas. The impact is further characterized by the Weber number ($We = \frac{U_0^2 D_0 \rho}{\sigma} = 750$), the Ohnesorge number ($Oh = \frac{\mu}{\sqrt{\sigma \rho D_0}} = 0.014$) and the dimensionless film thickness ($\delta = h_{f0}/D_0 = 0.2$). Besides the $\alpha = 70°$ case, also $\alpha = 60°$ and $\alpha = 50°$ are investigated.

Results and Discussion

In the case of a normal ($\alpha = 90°$) droplet impact onto a thin film the flow field is obviously rotationally symmetric. Roisman and Tropea [2] described the oblique impact by assuming a normal impact onto a flowing wall film, hence a symmetric stagnation point flow as an inner wall film and a constantly flowing outer wall film. A Galilean

transformation of their system back to an oblique impact on a stationary film still leads to a symmetric stagnation point flow.

The inner wall film flow is now investigated for an oblique impact ($\alpha = 70°$) on a stationary wall film with DNS. Figure 2 shows the velocity field of the liquid in the symmetry plane at $\tau = tU_0/D_0 = 2.0$. At that moment, the impacting droplet has already penetrated the wall film, was deformed and its liquid was redirected horizontally. For the inner wall film ($-1.2 < x/D_0 < 1.4$) a stagnation point flow can be recognized. For a more quantitative investigation, the velocity field from the DNS is further evaluated by averaging the velocity component parallel to the wall over the height of the wall film, $\bar{u}_r$. Figure 3 shows the velocity plotted over the radial distance r from the stagnation point for the front side ($x > 0$, $\varphi = 0°$) and the back side ($x < 0$, $\varphi = 180°$) for two moments in time. First of all, the graphs for $\bar{u}_r/U_0$ follow a linear progression. This means, that the radial velocity follows the assumption of a stagnation point flow $\bar{u}_r = a\,r$. The slope a is obviously the same in both azimuthal planes (front and back). Therefore, the DNS data confirms the model of a rotational symmetric stagnation point flow. Note that the factor a represents the strength of the stagnation point flow and it deceases with time, $a(\tau)$.

In summary, it can be said that the flow field inside the inner wall film shows that the analytical assumptions are also valid for an oblique droplet impact on a stationary wall film. The radial velocity, averaged over the film height, is described by $\bar{u}_r = a(\tau)\,r$ independent of the azimuth φ even for an oblique droplet impact. Note that the here described symmetry only applies to the velocity, however, not to the film height, which is addressed in the next paragraph.

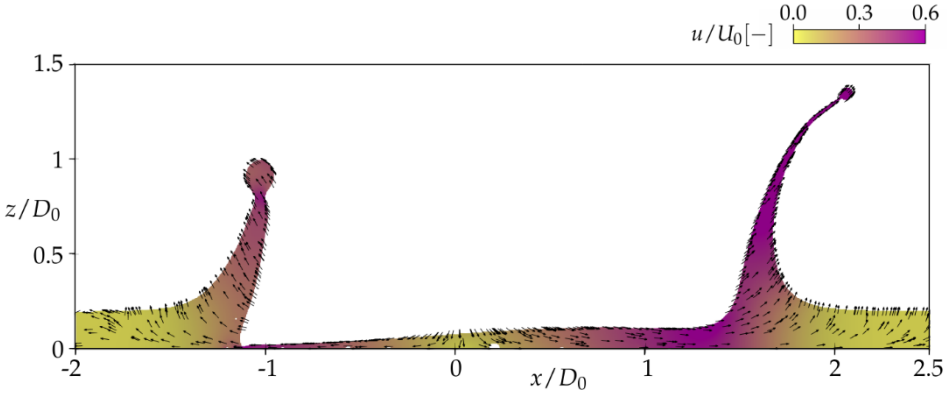

Figure 2. Velocity field in the symmetry plane at $\tau = tU_0/D_0 = 2.0$

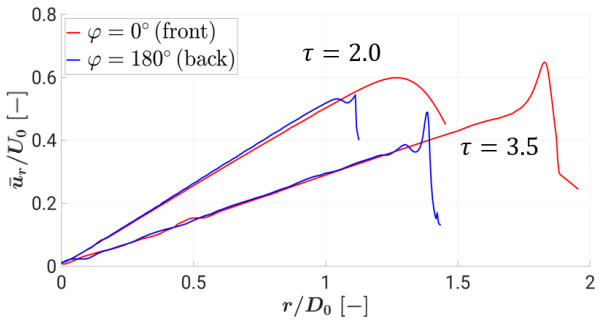

Figure 3. Velocity averaged over the film height plotted over radial distance from the stagnation point evaluated at two azimuthal planes ($\varphi = 0°, 180°$) at two moments ($\tau = 2.0, 3.5$).

The crown of an oblique impact is asymmetric in height as well as crown base radius as observed in Figure 2 as well as by several studies [4,5]. Since the velocity field is rotationally symmetric, as shown in the last paragraph, the asymmetry in momentum, which causes an asymmetric crown ejection, is attributed to the mass distribution of the impacting droplet. This is now investigated further.

The droplet and film fluid can be distinguished in the DNS. The computational domain is cut into 18 sections in azimuthal direction with a size of $\Delta\varphi = 10°$, e.g. $\varphi_1 = [0°, 10°] \approx 5°$, $\varphi_{18} = [170°, 180°] \approx 175°$. The centre is positioned at the stagnation point. The mass of droplet fluid is integrated within each section $m_{D,\varphi}$ and it is made dimensionless by referring it to 1/18 of the initial droplet mass. The red line in Figure 4 shows the mass distribution of the impacting droplet over all azimuthal sections. It is evaluated at $\tau = 1.0$ and it stays constant for later times. The maximum is located at the front ($\varphi = [0°, 10°]$). Here, the non-dimensional mass is $\tilde{m} = 2.0$, which means, that it is twice as high as for an equal mass distribution as observed during a normal droplet impact. The mass decreases monotonically with increasing azimuthal angle until a minimum can be found at the back with $\tilde{m} = 0.4$. A non-

dimensional mass of $\tilde{m} = 1.0$ is approximately present in section $\varphi = [70°, 80°]$. This means, that in this section the same amount of droplet mass is present as for a normal droplet impact with symmetric distribution. In general, it can be noted that the mass distribution is strongly asymmetric for this investigated oblique droplet impact scenario. In order to describe the asymmetry of the crown, the azimuthal distribution of the momentum transfer into the crown at its base is the relevant quantity to investigate. The momentum was evaluated at 80% of the inner crown radius, as visualized in Figure 5. An evaluation directly at the inner crown radius would lead to a distorted picture due to not only evaluating the momentum inflow into the crown but also the agglomerated momentum of the crown. The momentum transfer into the crown, $p_{\varphi i}$, was evaluated for each azimuthal section and integrated over time, $P_{\varphi i} = \int_{1.5}^{7} p_{\varphi i}\, d\tau$. Figure 4 shows the momentum distribution made dimensionless by the average over all sections, $\tilde{P}(\varphi i) = 18\, P_{\varphi i} / (\sum_{i=1}^{18} P_{\varphi i})$. It can be seen, that the momentum distribution matches precisely to the mass distribution as expected due to the symmetric velocity field.

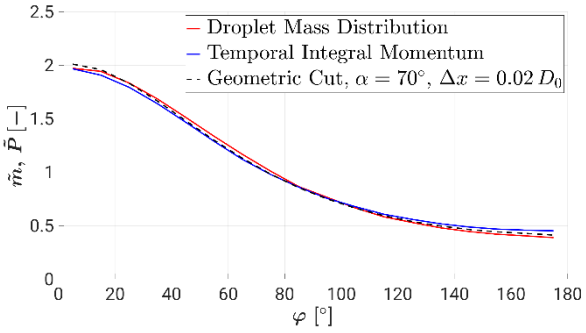

Figure 4. Dimensionless mass distribution of the impacting droplet into azimuthal planes φ, the dimensionless momentum distribution, and the volume distribution of a geometrically cut sphere.

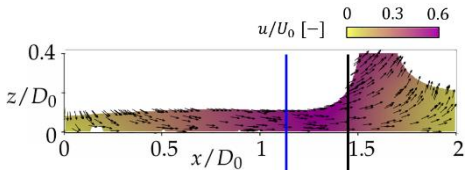

Figure 5. Velocity field in the symmetry plane visualizing the position for momentum evaluation (blue) and inner crown base radius (black).

In the following, a geometric formulation is presented to describe the mass and momentum distribution. It is motivated by the idea, that the stagnation streamline can be traced back to the moment of first contact of the droplet with the wall film. It is assumed that it forms a straight line though the droplet in an angle of $\alpha = 70°$. Each volume element of the initial droplet can then be assigned to the different azimuth section by its position in reference to this line. Figure 6 visualizes this with a slanted cylinder. The pink dashed line represents the stagnation streamline and is the center of the cylinder. The top and the bottom show the 18 azimuthal sections as described in the last paragraph. A sphere, representing the droplet at the moment of impact, can now be placed inside this cylinder at the origin of the coordinate system, as visualized by the yellow circle in Figure 6. The slanted cylinder is shifted in positive x-direction by Δx because the stagnation point in the DNS is also slightly shifted in x-direction. Each volume element of the sphere can now be assigned to an azimuth section. Or, in other words, the sphere is now cut by the azimuthal sections of the slanted cylinder. With that a volume distribution of the sphere in the azimuthal sections is obtained. The azimuth angle within the slanted cylinder as a function of its cartesian coordinates and the impact angle $\alpha \in (0°, 90°)$ is

$$\varphi(x, y, z) = arctan\left(\frac{z}{x + \Delta x + \frac{y}{tan(\alpha)}}\right). \tag{1}$$

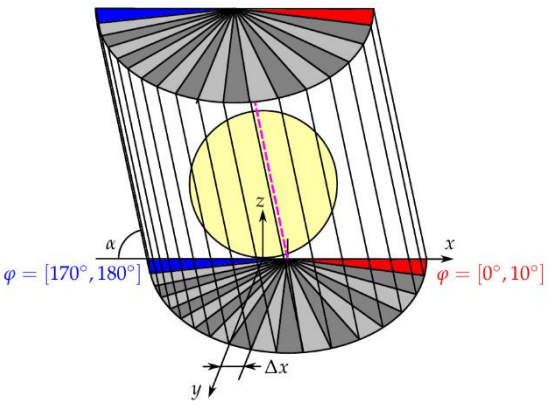

Figure 6. Visualization of a slanted cylinder consisting of 18 azimuth sections. It is slanted by an angle α and shifted by Δx in positive x-direction.

In Figure 4, the distribution of droplet volume by the cut into the azimuth sections is shown in the dashed line. It reproduces the measured distribution of mass and momentum from the DNS very accurately. With this simple geometric description, the mass distribution and momentum distribution of an oblique droplet impact onto a thin film a can be predicted by its impact angle and Δx, which is discussed in the next paragraph.
To further strengthen these findings, the same evaluations were made for more extreme oblique impacts with smaller impact angles. Figure 7 shows the droplet mass distribution, the momentum distribution, and the geometric distribution into the azimuthal sections for $\alpha = 60°$ (A) and $\alpha = 50°$ (B). The nondimensional momentum at the front ($\varphi = 0°$) is 2.6 for $\alpha = 60°$ and 3.4 for $\alpha = 50°$. This shows the increasing asymmetry of the impact with a decreasing impact angle. Also, for these lower impact angles the three distributions (momentum, droplet mass, geometric) match well. Only the shift Δx of the cylinder needs to be adjusted slightly to $\Delta x = 0.04\ D_0$ and $\Delta x = 0.07\ D_0$, respectively. This corresponds to an also further shifted stagnation point position x_{SP}. It, Δx, was found to be linked to the stagnation point position by $\Delta x \approx 0.6\ x_{SP}$.

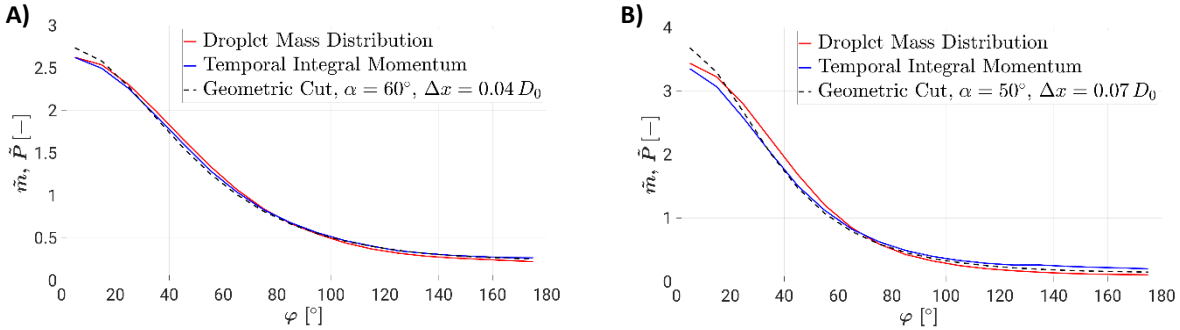

Figure 7. Droplet mass distribution, temporal integral momentum flux distribution, and geometric cut for $\alpha = 60°$ (A) and $\alpha = 50°$ (B).

Conclusion

This study showed that the flow field of the inner wall film represents a symmetric stagnation point flow even during an oblique droplet impact onto a thin wall film. The asymmetry in the momentum distribution results from the mass distribution of the impacting droplet. These both distributions over the azimuthal sections are the same and can be described by a geometric consideration of the intersection of a sphere with azimuth sections of a slanted cylinder. This makes it possible to predict the asymmetry of the inner wall film during an oblique droplet impact. In a next step, the resulting asymmetry of the crown could be further investigated.

References

[1] Yarin, A.L.; Weiss, D.A. Impact of drops on solid surfaces: self-similar capillary waves, and splashing as a new type of kinematic discontinuity. J. Fluid Mech. (1995), 283, 141–173
[2] Roisman, I.V.; Tropea, C. Impact of a drop onto a wetted wall: description of crown formation and propagation, J. Fluid Mech. (2002), 472, 373–397
[3] Eisenschmidt, K., Ertl, M., Gomaa, H., Kieffer-Roth, C., Meister, C., Rauschenberger, P., Reitzle, M., Schlottke, K., Weigand, B., Appl Math and Comp, 272-2: 508-517 (2016)
[4] Okawa, T.; Shiraishi, T.; Mori, T. Effect of impingement angle on the outcome of single water drop impact onto a plane water surface. Experiments in Fluids 2008, 44, 331–339
[5] Stober, J.L.; Santini, M.; Schulte, K. Influence of Weber Number on Crown Morphology during an Oblique Droplet Impact on a Thin Wall Film. Fluids 2023, 8, 301

Author index

Progetto grafico:
Servizi Editoriali – Università degli Studi di Bergamo
Università degli Studi di Bergamo
via Salvecchio, 19
24129 Bergamo
Cod. Fiscale 80004350163
P. IVA 0161280016